Naval Research Laboratory

Washington, DC 20375-5000

NRL Report 9099

Measurement and Interpretation of North Atlantic Ocean Marine Radar Sea Scatter

DENNIS B. TRIZNA

Radar Propagation Staff
Radar Division

May 31, 1988

SECURITY CLASSIFICATION OF THIS PAGE

REPORT DOCUMENTATION PAGE

1a. REPORT SECURITY CLASSIFICATION UNCLASSIFIED	1b. RESTRICTIVE MARKINGS
2a. SECURITY CLASSIFICATION AUTHORITY	3. DISTRIBUTION / AVAILABILITY OF REPORT Approved for public release; distribution unlimited.
2b. DECLASSIFICATION / DOWNGRADING SCHEDULE	
4. PERFORMING ORGANIZATION REPORT NUMBER(S) NRL Report 9099	5. MONITORING ORGANIZATION REPORT NUMBER(S)
6a. NAME OF PERFORMING ORGANIZATION Naval Research Laboratory 6b. OFFICE SYMBOL (*If applicable*) Code 5303	7a. NAME OF MONITORING ORGANIZATION Office of Naval Reserch
6c. ADDRESS (*City, State, and ZIP Code*) Washington, DC 20375-5000	7b. ADDRESS (*City, State, and ZIP Code*) Arlington, VA 22217-5000
8a. NAME OF FUNDING / SPONSORING ORGANIZATION Office of Naval Research 8b. OFFICE SYMBOL (*If applicable*)	9. PROCUREMENT INSTRUMENT IDENTIFICATION NUMBER
8c. ADDRESS (*City, State, and ZIP Code*) Arlington, VA 22217-5000	10. SOURCE OF FUNDING NUMBERS PROGRAM ELEMENT NO. 61153N; PROJECT NO. RR021-05-43; TASK NO.; WORK UNIT ACCESSION NO. DN280-045

11. TITLE (*Include Security Classification*)
Measurement and Interpretation of North Atlantic Ocean Marine Radar Sea Scatter

12. PERSONAL AUTHOR(S)
Trizna, Dennis B.

13a. TYPE OF REPORT	13b. TIME COVERED	14. DATE OF REPORT (*Year, Month, Day*)	15. PAGE COUNT
Interim	FROM Jan 85 TO Jun 87	1988 May 31	51

16. SUPPLEMENTARY NOTATION

17. COSATI CODES			18. SUBJECT TERMS (*Continue on reverse if necessary and identify by block number*)
FIELD	GROUP	SUB-GROUP	Radar; Remote sensing; Sea spikes; Radar clutter; Air-sea interaction

19. ABSTRACT (*Continue on reverse if necessary and identify by block number*)

Results are presented for experiments conducted with a noncoherent, high-resolution marine navigation radar aboard the NOAA ship *Researcher* in the North Atlantic Ocean. High-resolution radar backscatter data were collected under wind-wave equilibrium conditions, i.e., both fetch and time requirements for fully developed seas were satisfied for the wind speeds reported. Cumulative distributions of normalized radar cross section (NRCS) of the sea surface are calculated and found to follow two Weibull distributions. Based on their characteristics, the distributions may be ascribed to two different scattering mechanisms: one due to scatterers evenly distributed over the surface, such as Bragg scatter; one due to localized scattering features, such as wave crests. The percentage occurrence of the localized scattering events (often called sea spikes) behaves with wind speed in a manner much like that found for whitecaps. Other characteristics of the two distributions also appear to correlate with wind speed, with a weak dependence on air-sea surface temperature difference. For very low grazing angles, many of these characteristics vary sharply near the 2° depression angle, which is a critical angle in several scattering models. An additional scattering model is proposed here to explain this behavior.

20. DISTRIBUTION / AVAILABILITY OF ABSTRACT ☒ UNCLASSIFIED/UNLIMITED ☐ SAME AS RPT. ☐ DTIC USERS	21. ABSTRACT SECURITY CLASSIFICATION UNCLASSIFIED
22a. NAME OF RESPONSIBLE INDIVIDUAL Dennis B. Trizna	22b. TELEPHONE (*Include Area Code*) (202) 767-2003 22c. OFFICE SYMBOL Code 5303

DD FORM 1473, 84 MAR

SECURITY CLASSIFICATION OF THIS PAGE

CONTENTS

INTRODUCTION 1

EXPERIMENT DESIGN 1

Data Acquisition 1
Data Analysis Technique 3
General Behavior of the Data 6

RESULTS 6

NRCS Median vs Wind Speed 7
Depression Angle Dependence of 10-m/s Fitted Value 8
Empirical Model 8
Percentage Value of Sea Spikes 10
A Model for $U_w^{3.75}$ Wind Speed Dependence 13
Effects of Shadowing of Small Crests 14
Reconciliation of $U^{0.5}$ and U^1 Dependences of Drag Coefficients 14
Sea Spike RCS vs Wind Speed 15
Effective Mean of the Sea Spike Region vs Wind Speed 15
Mean Sea Spike NRCS at 10 m/s 15
1% Sea Spike Intercept 15
Sea Spike Model for RCS Depression Angle Characteristics 15
Distributed-Scatter Weibull Shape Parameters 23
Sea Spike Scatter Weibull Shape Parameters 24
Median NRCS vs Friction Velocity for Four Drag Coefficients 24

RELATED EXPERIMENTS 29

Airborne Coherent Doppler Measurements 29
Dual-Polarized Measurements 29
Doppler Spectrum Peak Shift Model 31
Doppler Spectra 31
Open Ocean X-Band Doppler Spectra 31
Summary of Experiments—Properties of a Doppler Shift Model 33

SUMMARY 34

ACKNOWLEDGMENTS 36

REFERENCES 36

APPENDIX A — Low Grazing Angle Sea Scatter Background 39

APPENDIX B — Air-Sea Interaction Parameterization 45

MEASUREMENT AND INTERPRETATION OF NORTH ATLANTIC OCEAN MARINE RADAR SEA SCATTER

INTRODUCTION

The study of radar sea scatter for moderate to high grazing angles has received much attention over the past several years because of airborne and spaceborne remote sensing and military tactical applications. The low grazing angle case, on the other hand, has received far less attention. This case is more complicated for several reasons, including the effects of shadowing of the surface by wave crests; the occurrence of high-amplitude transient returns referred to as sea spikes [1-4]; and the wider range of sea echo strengths expected for these very low grazing angles as a result of modulation of the local incidence angle by the slope of the long wave. With the development of more sophisticated Navy shipboard radars, it has become apparent that a satisfactory sea clutter model for such radars is lacking, thus warranting experimental work in this area. In addition to clutter model applications, the shipboard marine navigation radar has recently received attention as a potential tool for remote sensing of the ocean surface by using its surface-imaging capabilities [5,6].

In the work reported here, statistics of the normalized radar cross section (NRCS) of the sea surface were determined by using a large number of hourly measurements from a shipboard marine navigation radar. The data were collected from the NOAA research vessel *Researcher* by using a horizontally polarized, high-resolution X-band radar operating at grazing angles between 1° and 7°. (For this report, a radar is considered as high or low resolution if its pulse length is much less or much greater than the dominant ocean wavelength.) The amplitude statistics of the samples of the NRCS of the ocean surface were calculated from digitized measurements of the radar video signal for each of a series of range bins that were sorted by azimuth. Data from a 60° azimuthal sector were used, the sector being centered about the direction of highest radar scatter levels. These were generally found to be the same as the wind direction. Because of low digital recording rates, the data were collected using angle increments of several degrees in azimuth. Many antenna rotations were required to achieve uniformly filled azimuthal coverage. Thus, although the waves are not imaged as described in Ref. 5, statistics of the scatter from all portions of the long waves were sampled as the wave system traveled through a range bin for a given azimuthal sector over many antenna rotations.

Specifically defined parameters of the NRCS statistics are correlated against shipboard measurements of wind speed and air-sea surface temperature difference. From these quantities, wind stress is calculated and compared with the radar measurements, similar to the procedure used for airborne and spaceborne scatterometers. Applying these results to remote sensing of wind stress leads to a technique that uses a relatively low data rate and simple signal processing.

EXPERIMENT DESIGN

Data Acquisition

An experiment was designed to study low grazing angle sea scatter under open ocean conditions under joint Navy and NOAA cooperation. The NOAA research vessel *Researcher* was instrumented to collect radar sea scatter data by using one of its two Raytheon marine navigation radars, the antenna

Manuscript approved April 28, 1987.

of which is shown in Fig. 1. Although the Raytheon radar is not universally used on oceangoing ships, its design is typical of such radars, and it is worthwhile to discuss its operating parameters as they affect this experiment. The shortest pulse available from this system is 65 ns when used in its short-range mode. This mode also uses a 3.5 kHz pulse repetition frequency (PRF), which yields a 286-μs period between pulses. With a 1° antenna beamwidth, 18 pulses are transmitted while the antenna illuminates a target with a 1.8-s rotation period. In this mode, the 9.75-m pulse (65-ns pulse width) is much less than the typical open-ocean dominant wave length, and the radar can be considered as high resolution for sea scatter studies, according to the definition stated previously.

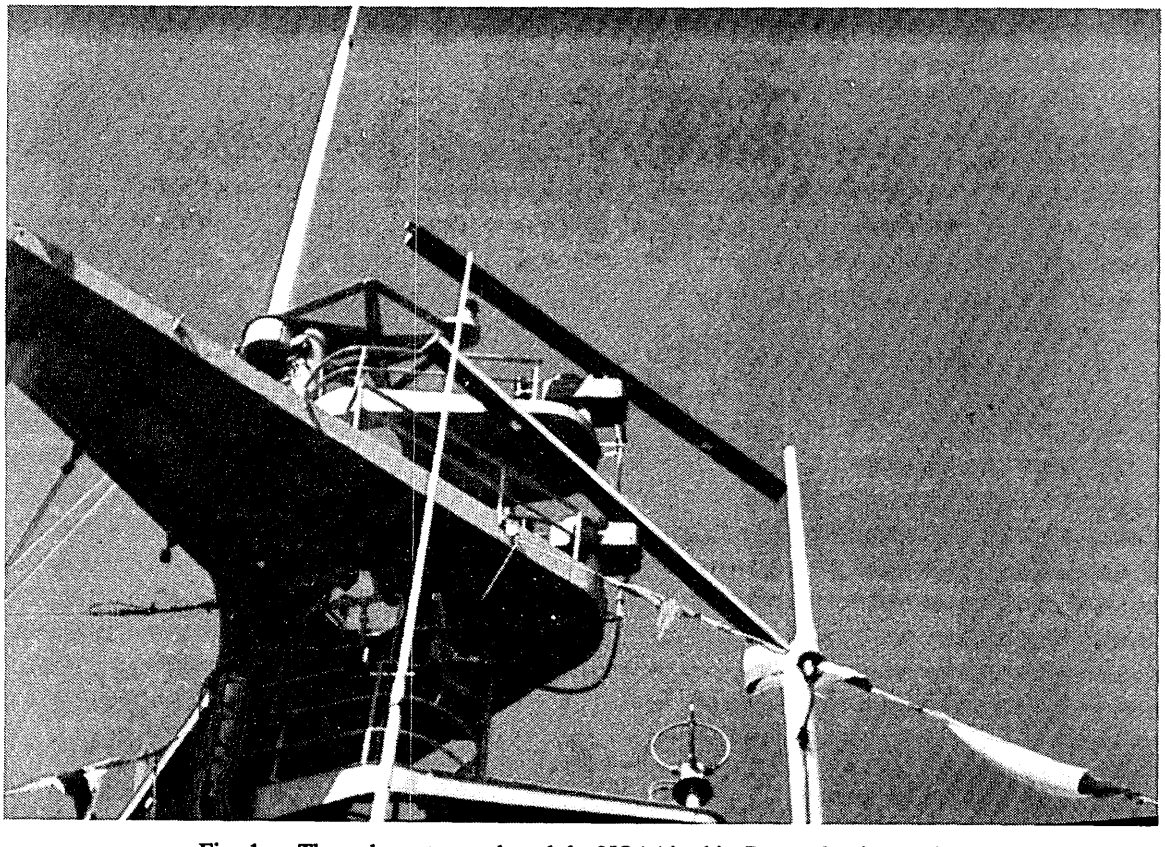

Fig. 1 — The radar antenna aboard the NOAA's ship *Researcher* is a typical marine navigation radar antenna, in this case made by Raytheon

A data acquisition system was interfaced to the output of the *Researcher's* marine navigation radars. It consisted of an HP-86 computer, a Tektronix 7612D transient waveform analyzer, and a Kennedy tape drive with a Dylon buffer interface. The various components were controlled by using an IEEE-488 GP-IB interface system. For this experiment, data processing was performed offline on a VAX-750 computer.

The radar was operated hourly in standard fashion on a not-to-interfere basis, except for selection of the minimum range display (discussed above) while recording data. The data were digitized with a 30-ns spacing over 256 samples per pulse, for a high-resolution measure of the sea-surface echo. These were recorded with an azimuthal spacing of 7°, determined by the tape drive speed, with 3400 records collected over 60 rotations of the antenna, taking about 2 min of each hour.

The system was calibrated by inserting a pulsed X-band signal generator output into the directional coupler at the radar transceiver box and incrementing through the 60 dB dynamic range of the receiver. Absolute calibration was then achieved by towing a radar calibration sphere (suspended from a weather balloon behind a boat) through the antenna beam while operating the antenna in a nonrotating mode. The tow line used was sufficiently long to allow separation of the boat's radar echo from the calibration sphere as the two passed successively through the antenna beam.

Data Analysis Technique

The first stage of sea-scatter data processing is sorting the samples according to antenna pointing direction. The radar sea echo maximizes symmetrically about the wind direction, and this echo maximum was used to select the region of scatter to be analyzed. Figure 2 shows an example of the range of received power encountered vs azimuth for one depression angle or range bin. Data from a 60° sector centered about the azimuth of wind-generated maximum scatter were chosen for statistical analysis for each of 10 range bin samples. These bins geometrically correspond to 10 depression angles, because the antenna pattern had essentially constant gain with elevation angle over the angles illuminated. This design maintains a uniform radar PPI display while the ship is pitching and rolling in high seas. Received-power data from this chosen azimuthal sector were first converted to normalized radar cross section (NRCS) for each data point by using receiver calibrations and the measured cross section of the calibrated sphere. Next, a cumulative histogram of NRCS was assembled for each range bin and plotted on Rayleigh probability paper. On such plotting paper, the Rayleigh distribution plots as a straight line with unit slope. The Weibull distributions plot linearly also, but the slope is a variable parameter defined by the distribution. The Weibull distribution yields a realistic fit for sea scatter [7-9] and allows parameterization of the NRCS distribution by using two variables. The cumulative probability density function of linear NRCS values x is represented by the Weibull distribution, parametric in A and B, and is given by

$$p(x) = \exp\{-(x^B) / A\}. \tag{1}$$

(See, for example, Ref. 10, p. 109.) The data are plotted as NRCS in dB vs the expected value, 10* log (x). From Eq. (1), this is log $[-\ln [p(x)] - \log A$. The Rayleigh probability axis is generated by substituting fractional values between, but not equal to, 0 and 1 (e.g., 0.999 and 0.001). On such Rayleigh paper, the slope of the straight line is B, which is also called the shape parameter. The parameter A is called the scale parameter. Both can be related to the mean value of the distribution μ by $\mu = A^{-B}\Gamma(B + 1)$, where Γ is the Γ function.

The distribution function of NRCS values

$$dp\,(x)\,dx = (B / A)x^{B-1} \exp\{-(x^B) / A\} \tag{2}$$

is the derivative of Eq. (1).

Figure 3(a) plots two theoretical Weibull distributions using Eq. (2) and the parameters listed, each with a different percentage scaling factor. Figure 3(b) shows a composite plot of these two distributions, consisting of one of the distributions in one percentage region and the second distribution in the second region. The cutoff between the two distributions is obvious. The distributions were generated on a linear NRCS basis, but they are plotted vs the log of NRCS, as with real data. This plot is shown to illustrate the reason for plotting the cumulative distribution rather than the probability distribution for the data. When plotting the probability distribution, it is not a simple matter to differentiate between the two distributions for two reasons. First, the higher amplitude contribution

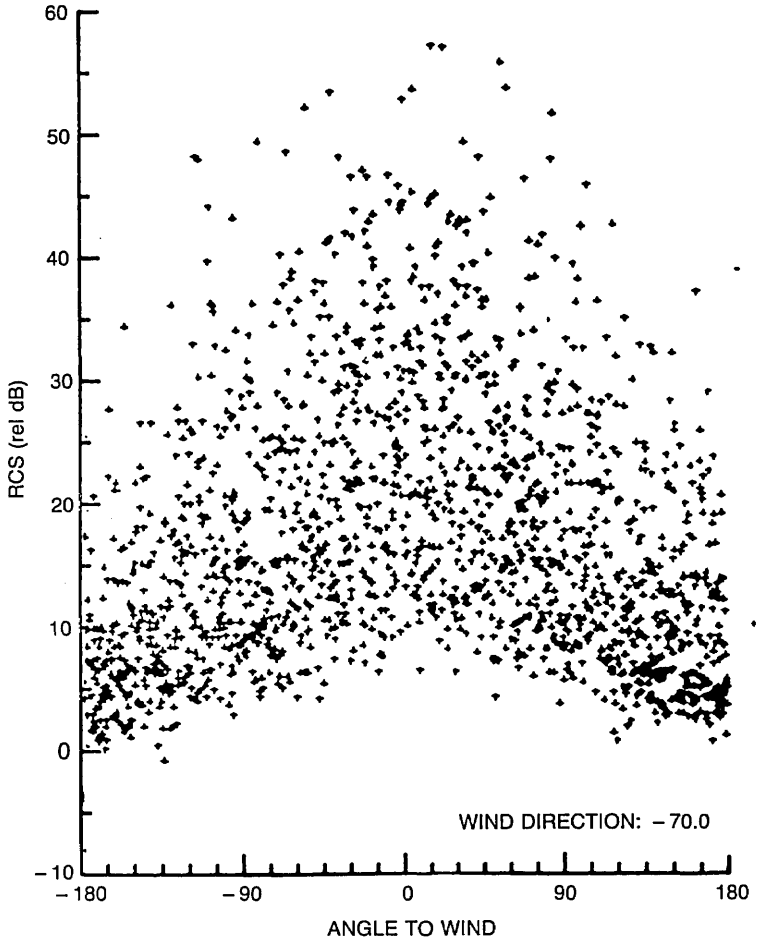

Fig. 2 — The amplitude distribution of received power of low grazing angle sea scatter is shown as a function of azimuthal angle. This peak in azimuth is probably determined by the direction of the large scale waves, typically coincident with the wind direction, but it can lag the wind direction under changing conditions.

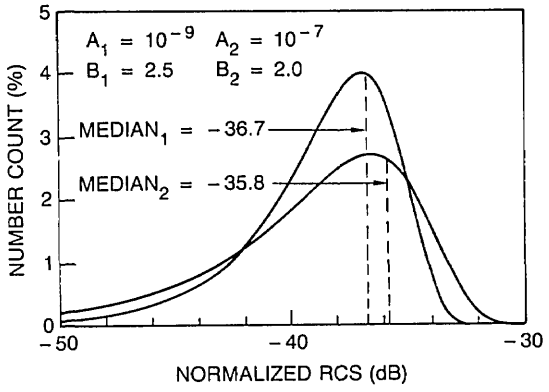

Fig. 3(a) — A pair of Weibull distributions generated from Eq. (4) by using the Weibull parameters

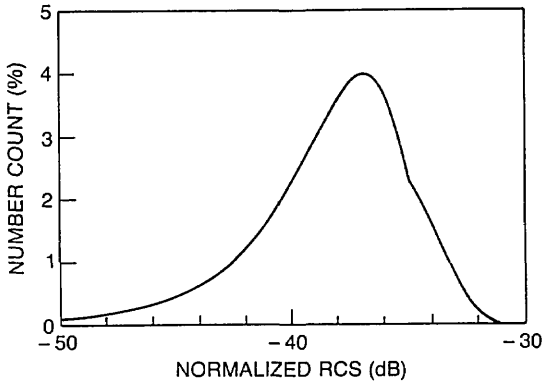

Fig. 3(b) — A single distribution created from using each of the distributions of Fig. 3(a). With such a distribution of real data, the break in the curve would be difficult to identify using the PDF due to inherent noisiness.

generally consists of a few to 40% of the data, and the peak location is simply not present in the composite plot. Second, because of the general noisiness of real data, the break point of transition of one curve to the other (evident in Fig. 3(b)) is not obvious either. However, because of the markedly different tails of the two distributions, the cumulative plot on Rayleigh paper allows this differentiation between Weibull distributions to be made relatively easily, with as little as 5% of the data points in the highest amplitude contribution. Note that simply adding the two distributions does not provide a pair of straight lines on the Rayleigh paper; it provides a curve with a hyperbolic shape near the transition from one Weibull to the other. To achieve two intersecting straight lines, as evidenced in the data, the first distribution must be held up to the level of intersection of the two curves, at which point the second distribution is in effect. It is as though one type of scattering feature simply replaces the first over an appropriate percentage of the surface, affecting the NRCS distributions accordingly.

Figure 4 shows the result of plotting three typical cumulative distributions of NRCS values for a single elevation angle (radar time delay) for low to moderate winds on Rayleigh paper. For the second and third case, there are three different regions of the plotted data, the highest two of which are fitted by straight lines. For very low wind conditions, the regions to either side of the middle linear region disappear, resulting in a single Weibull distribution.

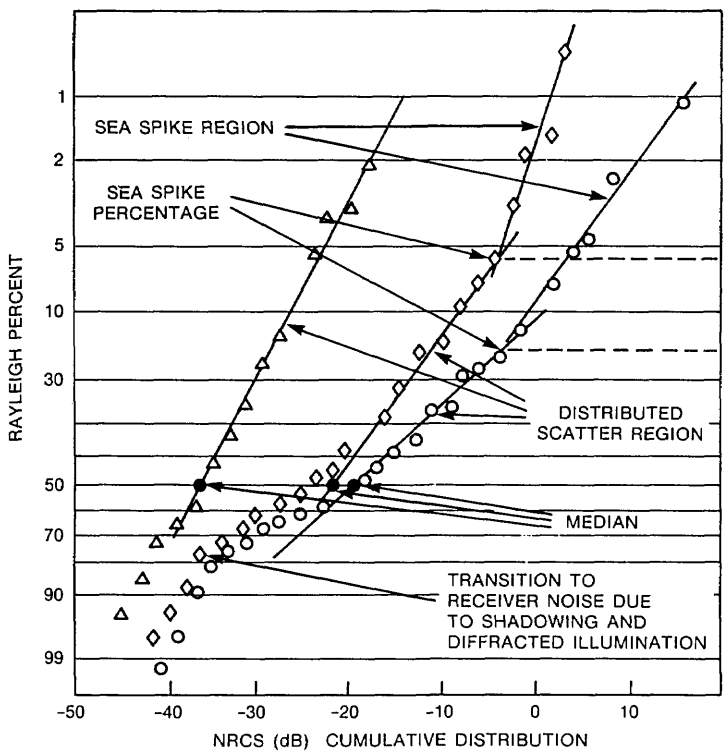

Fig. 4 — A cumulative probability distribution of sea surface NRCS data points. The resulting function appears bimodal, with the high NRCS region identified as sea spikes and the middle NRCS region identified with a distributed scatter source, such as Bragg scatter.

Software was developed for least-squares fitting of straight lines to both linear regions of the cumulative distribution, beginning with the high NRCS region. The linear fits to these two regions were defined for postanalysis by six parameters: (a) a slope (or shape parameter) B and (b) a 50% intercept for the lower amplitude line; (c) the NRCS amplitude and (d) percentage value of the intersection of the two fitted straight lines; and (e) the slope B, and (f) the "effective mean value" of NRCS of the higher amplitude straight-line fit. This effective mean value is taken as the decibel-mean of the NRCSs at the two-line intersection and the 1% intersection of the high-amplitude-region linear fit. These results provide a complete statistical characterization of the data and are stored for later correlation with surface truth parameters.

General Behavior of the Data

Before comparing radar and environmental data, some of the characteristics of the data should be interpreted in light of possible scattering mechanisms. The higher amplitude contribution in Fig. 4 are associated with so-called radar sea spikes, which have been identified in previous experiments [1-4]. In these experiments, the radar was not rotating but illuminated the same patch of sea surface continuously. The term sea spike is used because of the temporal behavior of certain periods of the radar return. During these periods, the signal is much stronger and has a short-term amplitude variation. This variation is much less than the scatter signal that varies in a periodic manner and is similar to that of the sea surface. Thus sea spikes are expected to occupy the highest amplitude region of the probability distribution.

Although they have been studied for shoaling conditions near shore by Kalmykov and Pustovoytenko [11] and the NRL group [1-4], except for the work of Hansen and Cavaleri in the Gulf of Mexico [12], few deep-water experiments have been conducted. The observations of Hansen and Cavaleri have deterministically associated high-amplitude radar returns with white-water features around the crests of waves. These observations have been made by using split-screen visual presentations of the radar cell and the amplitude time sequence of the received echo power. In Weibull fitting of their data, they also showed a break in the high-amplitude region but did not deterministically associate individual contributions to the distribution with specific echos in time. We assume that the higher amplitude distribution in our data is also caused by crest features. This assumption is verified by the behavior of the data with increasing scattering area.

The behavior of the data in the lowest amplitude region of Fig. 4 looks similar to the tail of a Gaussian distribution when plotted on Rayleigh paper. We suggest that this region contains samples of receiver noise that result for data samples recorded at time delays occurring in the shadowed area of the radar illumination, just behind the wave crest. This is discussed in Appendix A. This feature is found to disappear for very low winds and waves, as would be expected as shadowing diminishes.

The middle region for depression angles $>2°$ generally encompasses the majority of the data samples. This region may be associated with the major fraction of the illuminated surface, where a composite-scatter model would be expected to hold when a distributed scattering mechanism is dominant. This region reduces to the single distribution found for mild winds when shadowing and wave breaking are minimal. Further evidence for these preliminary interpretations follows.

RESULTS

For correlation with the radar data, environmental measurements were made of temperatures of the air and seawater, as well as wind speed and direction. Wind speed was measured by an anemometer at a height of 30 m on the ship's forward mast. Wet and dry bulb air temperatures were measured hourly on the bridge. Seawater temperature was measured by a water intake port at the bow of

the ship at a depth of ~2 m. Data were collected throughout a 6-day period in a region ranging from long. 40° to 42° W and lat. 71° to 72° N, off the coast of Long Island, New York. Results are shown in Fig. 5.

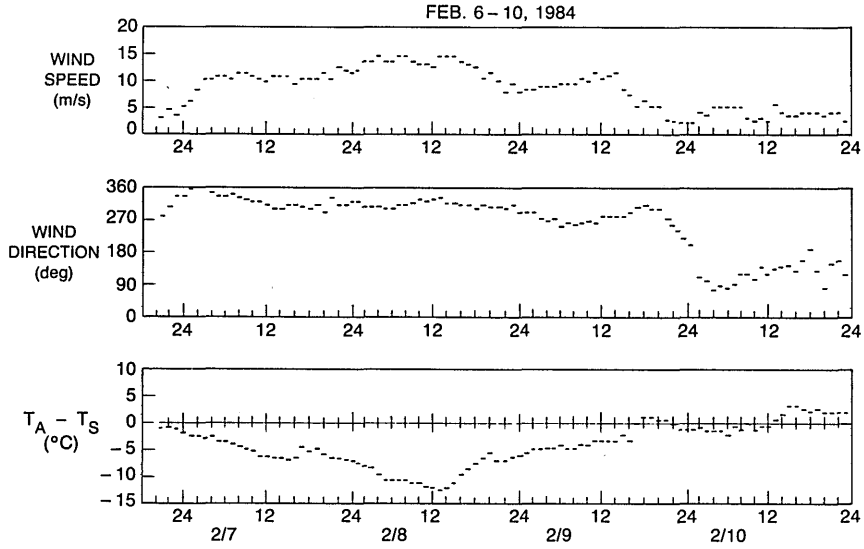

Fig. 5 — A plot of the environmental parameters measured aboard the NOAA ship *Researcher* for the days covered by the experiment. The days covering the radar data show a relatively constant wind direction throughout the period.

During the 6 days, the first 3-day period featured winds blowing from 2 to 18 m/s from the northwest, off the coast of Long Island, resulting in a minimum fetch of 185 km. On the fourth day, the winds changed direction by 180° as a result of the passage of a front. This gave radar results that differed markedly from the first 3-day period because of confused seas. On 10 February, additional low-wind-speed data were available for analysis as well, before a slow and continuous change occurred in wind direction. The radar data for the period of changing winds show a great deal of scatter, representing a nonequilibrium condition between winds and waves. We consider here only the cases for near-equilibrium conditions, using data collected during the period between 7 February and 1900 local time on 9 February, and for a short period on 10 February.

The reduced NRCS distribution parameters described earlier are first compared with wind speed. The data are differentiated according to air-sea temperature differences, with different plotting symbols used for 2° increments in temperature [13]. Results for the various NRCS parameters variation with wind speed follow.

NRCS Median vs Wind Speed

Consider first the variation of the 50% intercept, or median, of the cumulative distribution for individual incidence angles. (Note that this median generally is also the median of the midlevel distribution, unless the high-level region exceeds 50%.) The median is plotted vs wind speed in Fig. 6 for four of the 10 processed range bins corresponding to depression angles of 1.0°, 1.3°, 1.6°, 2.0°, 2.4°, 3.1°, 3.8°, 5.1°, 6.6°, and 7.7°. (These angles were chosen for analysis to provide a logarithmic variation in depression angle spacing.) Each set of points has been least-squares fit to a straight line. The slope, variance, and 10-m/s wind speed intercept is shown at the bottom of each figure. (Note that this linear fitting corresponds to conventional treatment of depression-angle variation of NRCS, both in the area of scatterometry and low-grazing-angle sea-scatter modeling. It

presupposes a power-law dependence of NRCS on wind speed, an assumption being reconsidered in some circles). A comparison with previous measurements of Sittrop [14], who used a pulse length of 120 ns and HH polarization shows excellent agreement with our results. This pulse length is roughly twice the value of ours but is still in the high-spatial-resolution regime, as defined earlier.

The last two depression angles, 6.5° and 7.7°, correspond to time delays that are affected by the time-dependent receiver attenuation known as sensitivity-time-control (STC), which is used to protect the receiver from leak-through of the transmitted pulse. Although the slope of median NRCS vs wind speed is valid for these two depression angles, the absolute values should be scaled upward by an unknown amount, since receiver calibrations are performed at longer time delays.

Depression Angle Dependence of 10-m/s Fitted Value

The results of the linear fits of Fig. 6 have been summarized in Fig. 7 in the form of the dependence of the intercepts and slopes on the depression angle. For the 10-m/s intercepts of NRCS, note the very weak depression angle dependence, with just four decibels separating the first value from the eighth. This agrees with the distributed scatter arguments made earlier. The last two angles now show more quantitatively the effects of the STC attenuation discussed earlier. The error bars on each point are the standard errors of the linear fits. The results of Fig. 7(a) are fitted by eye to a straight line, with a 0.45 slope on the log-log plot.

Figure 7(a) shows that the NRCS values occupy similar amplitude levels from one grazing angle to the next and exhibit similar slopes at the lowest grazing angles. This apparent similar NRCS variation over these five lowest depression angles can be described by one of two different models. Either the median NRCS is independent of both illuminated area and grazing angle or the NRCS variation with each of the two parameters causes their mutual cancellation, probably a less likely phenomenon. The Bragg-scatter basis of the composite scatter model predicts area independence of the NRCS. However, the NRCS values and the weak incidence-angle dependence is definitely not in agreement with the evidence discussed in Appendix A for horizontal polarization. (Again with the caveat that medians for high-spatial-resolution data and means of low-spatial-resolution data are not necessarily comparable.) The very weak variation of NRCS with increasing radar cell size gives evidence for a distributed surface scattering mechanism in the midamplitude region. Therefore we refer to this scatter as the distributed scatter region.

Figure 7(b) shows a plot of the slopes of Fig. 6 vs wind speed. These results for the last two angles are valid now, since the change of the median NRCS with wind speed is independent of STC attenuation. It also shows that the shadowing is not affecting the median NRCS-wind speed slope vs depression angle.

Empirical Model

For engineering design interests, an empirical model can be formulated to summarize the results of the last two figures. A straight line has been fitted to the data of Fig. 7:

$$\log [\mathrm{NRCS}_{10\mathrm{m/s}}(\theta)] = -3.18 + 0.45 \log [\theta(\mathrm{deg})], \tag{3a}$$

$$m(\theta) = 2.5 + 5.0 \log (\theta(\mathrm{deg})) \qquad 1 < \theta < 4.5 \tag{3b}$$

$$= 6.5 \qquad 4.5 < \theta < 7.7.$$

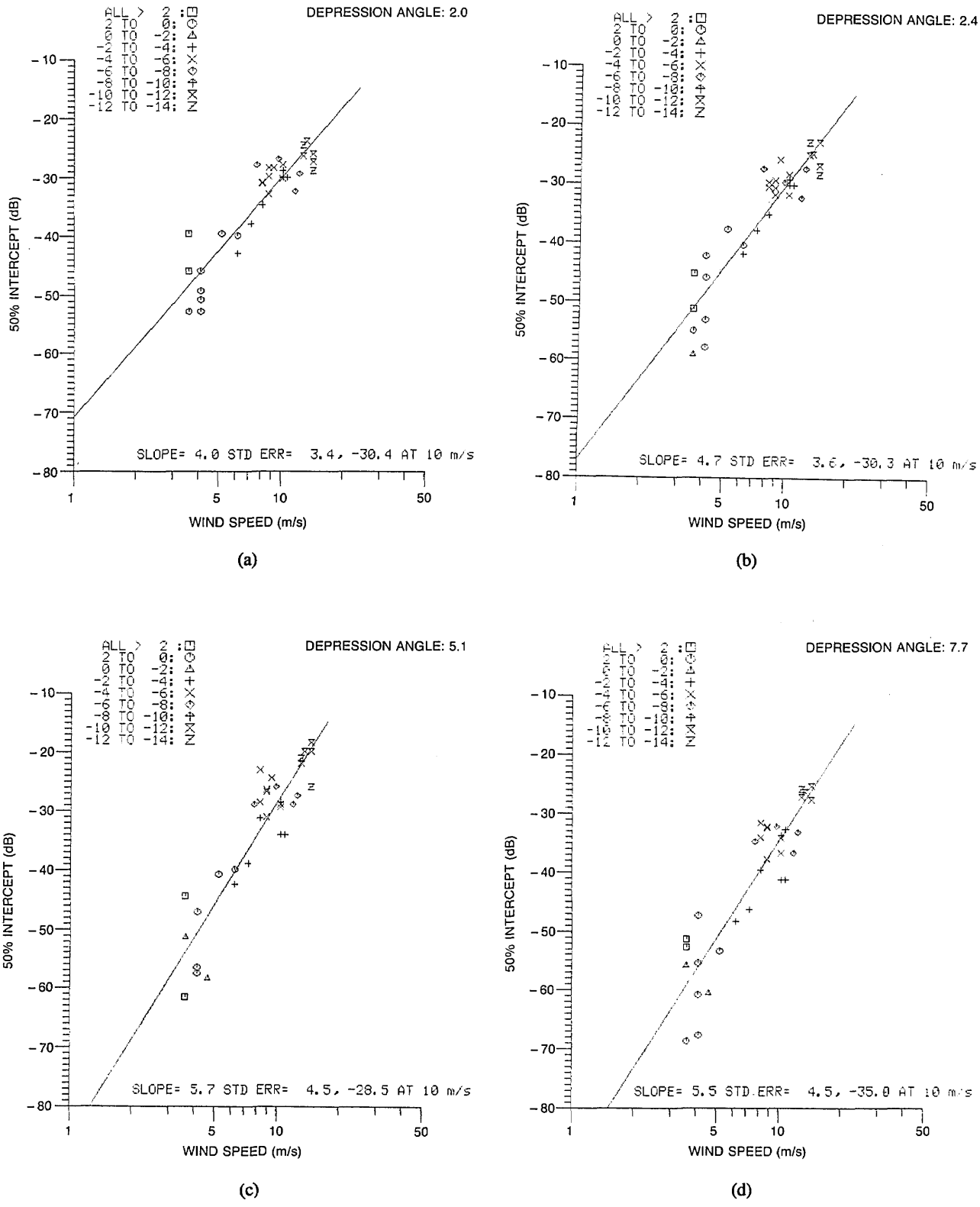

Fig. 6 — The 50% intercept, or median value, of the hourly radar scatter measurements plotted vs wind speed for 4 of 10 radar depression angles for the period covering 2/6 (2100) to 2/10 (2100)

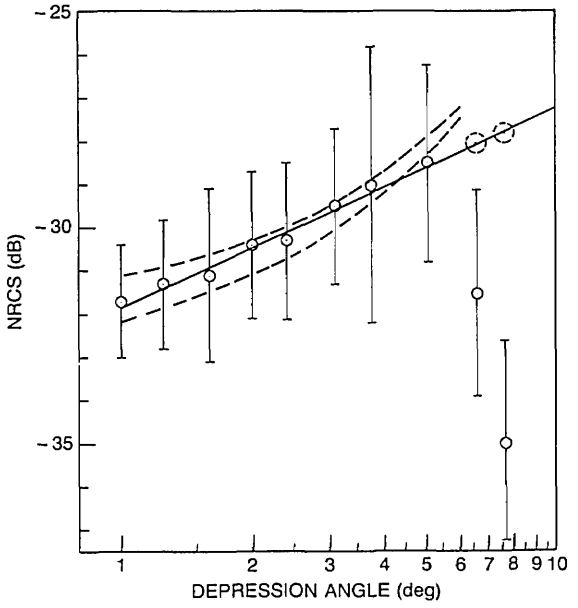

Fig. 7(a) — Distributed scatter NRCS value at the 10-m/s intercept plotted vs radar depression angle. The last two points show the effects of the radar STC circuit at the shortest ranges sampled. The two curves were calculated using the composite scatter model with tilt modulation, adding a mean surface slope of 16° and 20° to each depression angle labeled on the x-axis.

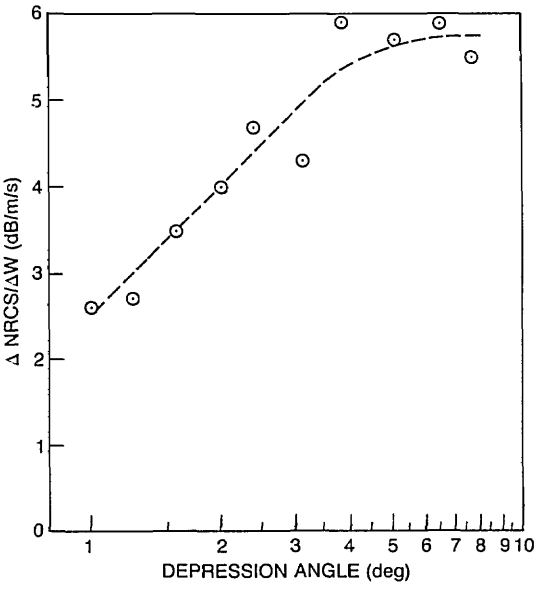

Fig. 7(b) — The slope of the linear fits of Fig. 8 plotted vs radar depression angle, indicating the wind speed variation of the NRCS change for each angle

The variation of the median NRCS of the distributed scatter is thus given by:

$$\log (\mathrm{NRCS}_{\mathrm{med}}/\mathrm{NRCS}_{10\mathrm{m/s}}) = \mathrm{m}\ (\theta)^{*}\ \log\ (U_w/10) \tag{4}$$

where U_w is the wind speed measured aboard ship.

Percentage Value of Sea Spikes

The next parameter to consider is what may be viewed as the percentage occurrence of sea spikes, defined by the value of the intersection of the two fitted lines on the Rayleigh paper, indicated by the dotted lines in Fig. 4. This percentage value can also be considered as the fractional percentage of NRCS values associated with the higher amplitude linear-fit region of the data. Results for the 10 depression angles presented above are plotted vs the log of wind speed (Fig. 8). This time, a line of 3.75 slope has been drawn through the data, based on a model for wave-breaking occurrence to be discussed later. No attempt has been made to optimize the fits by choosing an appropriate origin for each case, and the intercept at 100% occurs at ~10-m/s wind speed.

It is apparent that the data for the higher grazing angles more closely fit a 3.75 slope than those for lower grazing angles. This is expected because the percentage occurrence of sea spikes is a function of both the occurrence of scatterers on the surface and the occurrence of shadowing. Shadowing is expected to have a stronger effect at the lowest depression angles for high waves. That is, for the higher wind speeds, sharper crested waves will produce more shadowing at the lowest grazing angles, thus reducing the observed percentage occurrence of sea spikes.

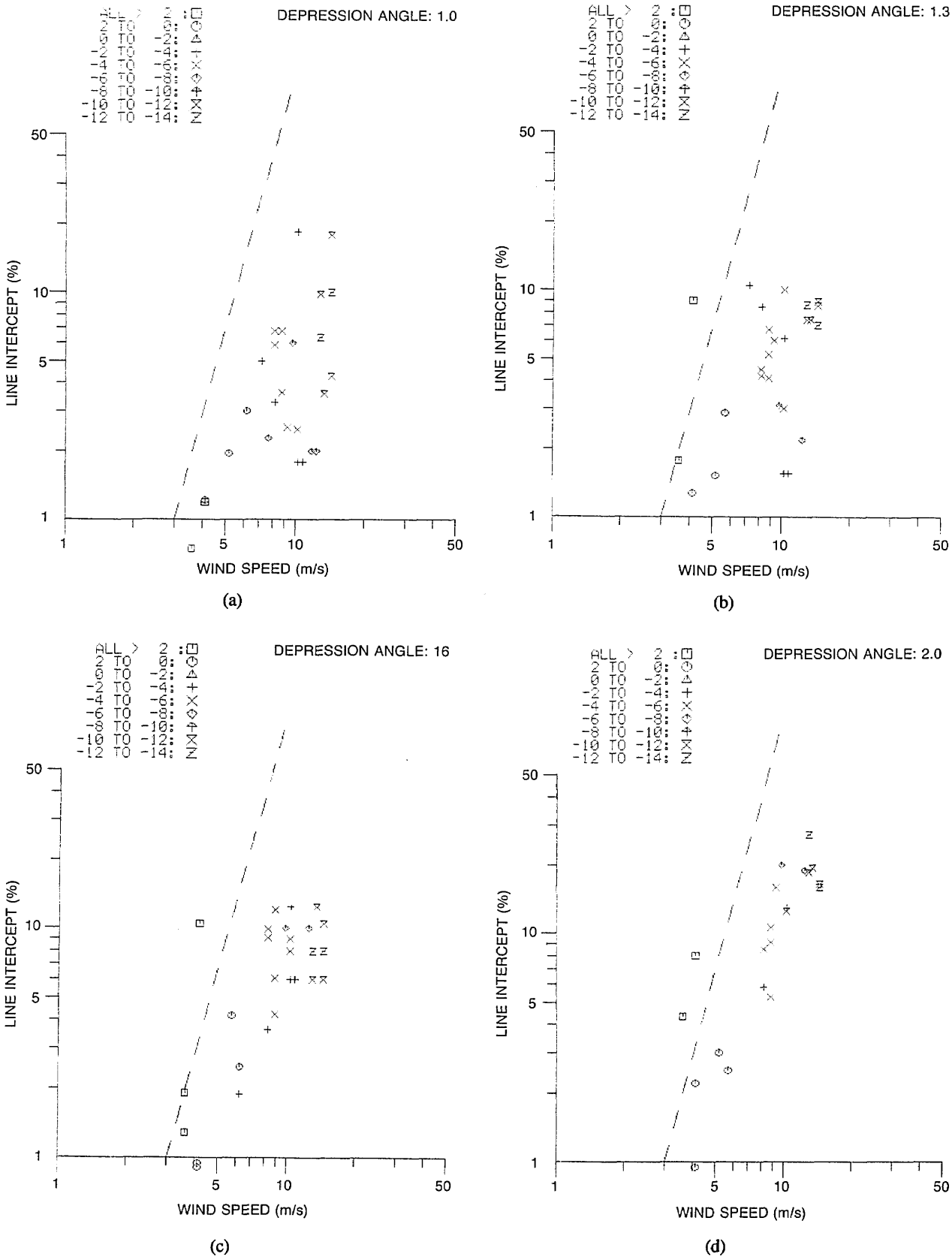

Fig. 8 — Plots of the percentage coordinate of the intersection of the two linear fits, interpreted as the percentage occurrence of sea spikes, plotted vs wind speed for the 10 radar depression angles. For angles <2°, the high-wind-speed results fall below the dotted line, perhaps as the result of shadowing, as discussed in the text.

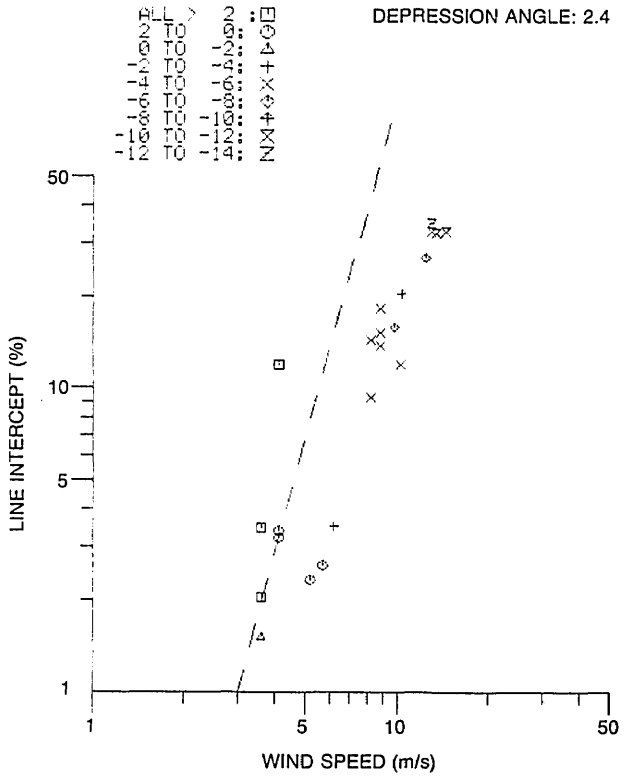

(e)

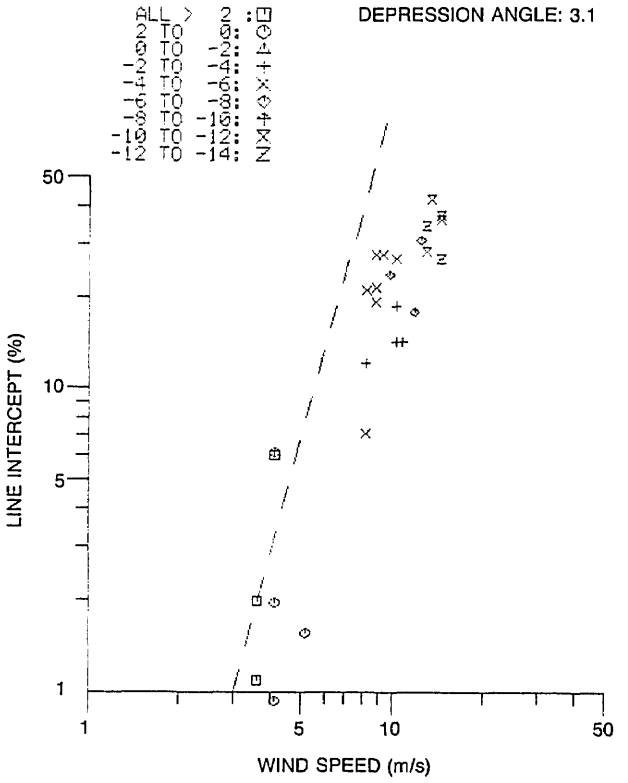

(f)

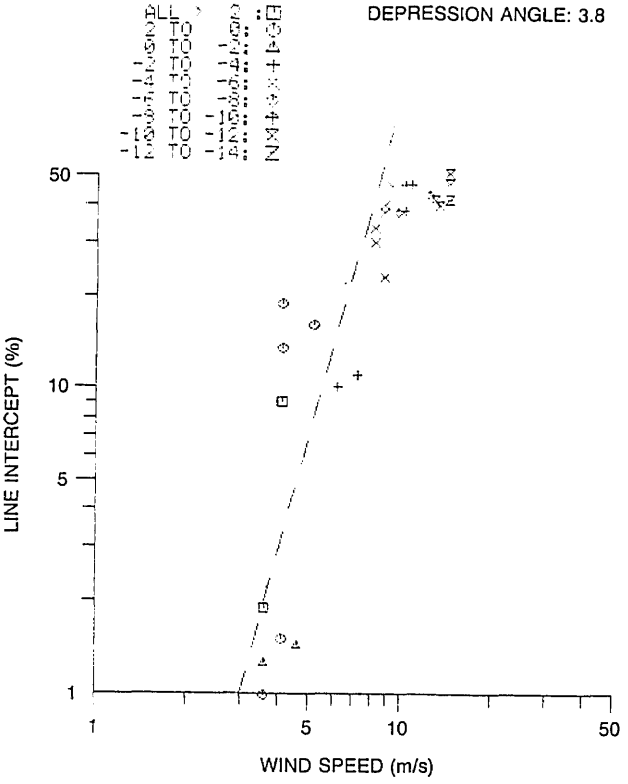

(g)

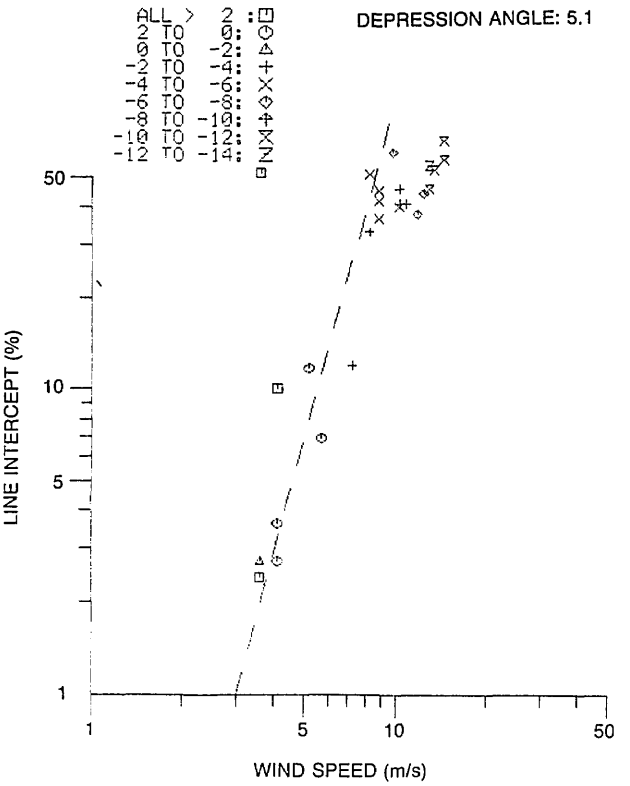

(h)

Fig. 8 — (Continued) Plots of the percentage coordinate of the intersection of the two linear fits, interpreted as the percentage occurrence of sea spikes, plotted vs wind speed for the 10 radar depression angles. For angles $<2°$, the high-wind-speed results fall below the dotted line, perhaps as the result of shadowing, as discussed in the text.

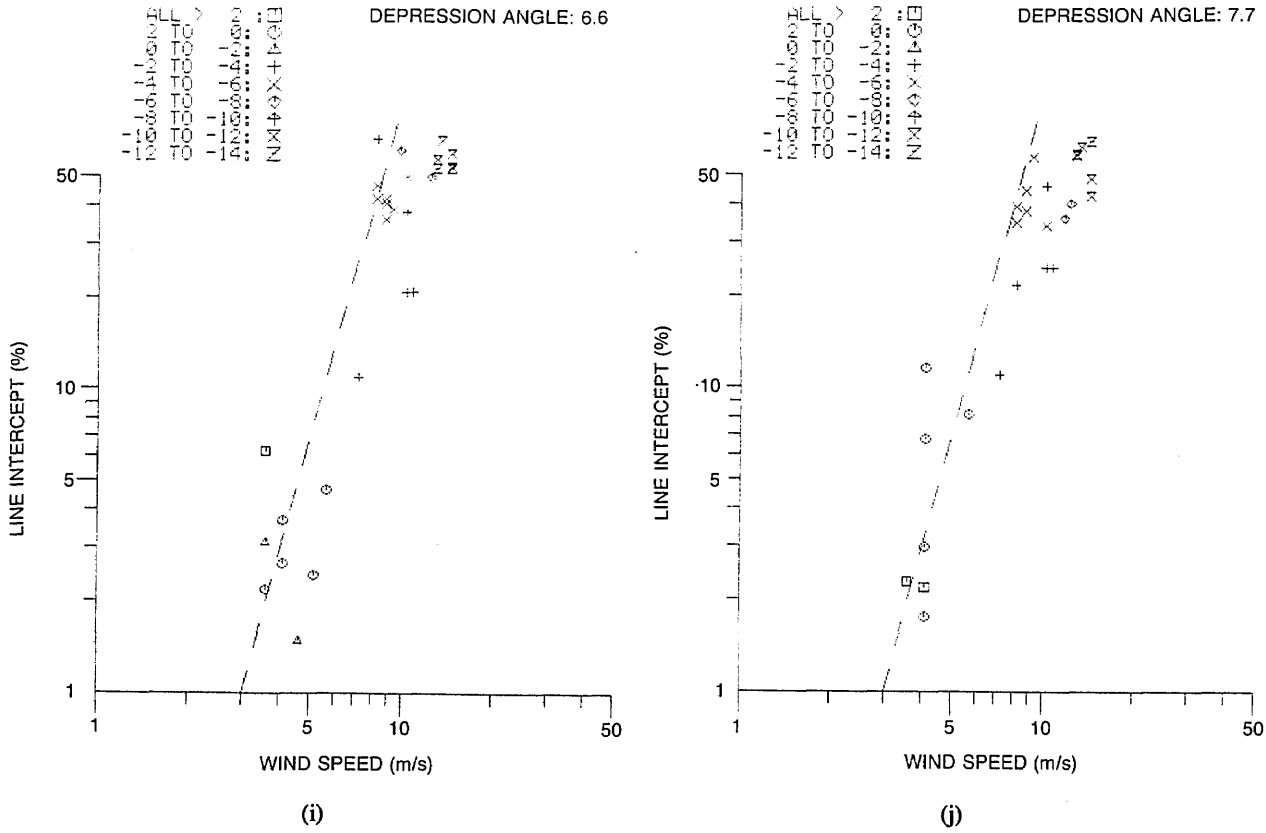

Fig. 8 — (Continued) Plots of the percentage coordinate of the intersection of the two linear fits, interpreted as the percentage occurrence of sea spikes, plotted vs wind speed for the 10 radar depression angles. For angles $<2°$, the high-wind-speed results fall below the dotted line, perhaps as the result of shadowing, as discussed in the text.

Although there is much scatter in the data and not all air-sea temperature ranges are available for all wind speeds, a weak trend in temperature effects is discernible, but the expected scatter in wind speed precludes drawing any firm conclusions for this parameter. The wind speed error is discussed in greater detail later.

A Model for $U_w^{3.75}$ Wind Speed Dependence

Consider the apparent $U_w^{3.75}$ dependence of the percent-intercept of Fig. 8. Hansen and Cavaleri [12] provide evidence that radar sea spikes are associated with features near the crests of waves, particularly those crests that are nearly or actually breaking. Whitecap coverage is also associated with breaking waves and the residual white water. Thus, the percentage occurrence of whitecap coverage and the percentage occurrence of radar sea spikes are expected to scale in a similar manner because they are both related to breaking or nearly breaking waves. As discussed in Appendix B, Wu [18] derived a model predicting a 3.75-power wind-speed dependence for whitecap coverage data, which is the reason for the 3.75-slope line plotted over the sea spike data reported here. Thus, the reason for this 3.75-slope fit is a theoretical one, implicitly associating percentage of radar sea spikes with percentage whitecap coverage as events with a common physical origin but without attempting to relate the proportionality factor between the two at this time. Further radar experiments are planned to determine whitecap coverage.

Effects of Shadowing of Small Crests

For grazing angles $>2°$, the fit of the data to the line is good. For angles of $\leq 2°$, either shadowing of the surface is affecting the fit for the higher wind speeds or a different scattering or propagation phenomenon is affecting the data. Shadowing could be expected to cause the observed reduction of sea spike percentages at high winds and steep waves for the lowest depression angles. It would do this by reducing the radar illumination of smaller crests on the steep forward face of the dominant wave that occur as a result of breaking (the spilling breakers considered by Wetzel [20]). (Appendix A describes this low-grazing-angle sea-scattering background. Figure A1(c) shows the sea surface illuminated for a very low grazing angle.) For this extremely low depression angle, only the crests of the dominant waves are being illuminated. For weaker winds, less developed seas, and the same depression angle shown in Fig. A1(c), the highest crests would not be as steep. This would cause less shadowing, and a higher fraction of crests present on the forward face of the longest waves would be illuminated. Thus, for a given radar depression angle, the fraction of wave crests on the surface that are not shadowed is dependent on long wave steepness, and implicitly, on the wind speed and time which it has blown.

For Figs. 8(e) through 8(j), apparently all crests are still illuminated for the wind speeds reported and shadowing reduces illumination only of the distributed scattering surface area. This increases the percentage value at which the top of the cumulative distribution of Fig. 3 rounds off to noise samples but only at the expense of number of samples of distributed scatter. At 2°, it appears as though there is a transition region to shadowing of smaller wave crests, since the data for the lower wind speeds lie reasonably close to the 3.75-slope line, and the waves for these winds still allow most of the crests present to be illuminated.

Predictions of scattering effects occurring near 2° have been published in the literature. Radar propagation effects near this angle have also been observed, such as the observed change in range falloff of NRCS from R^{-4} to R^{-8} (see, for example, Long [17]). This effect has previously been suggested as being the result of interference effects between the forward scattered wave and the direct wave, assuming geometric optics holds. Wetzel has proposed a shadowing function for low-grazing-angle scatter to explain such propagation effects [16]. The model suggests effective "islands of scatter" as a result of large crest shadowing. These islands are just the peaks of the dominant waves in his simplified formalism. He has suggested that this mechanism is responsible for the change in range dependence near the 2° depression angle. The only assumption Wetzel makes about the sea surface is one of mean slope appropriate to a fully developed sea. We suggest here that the percentage sea spike falling below the dashed lines for the lowest grazing angles in Fig. 8 is also a result of the onset of shadowing of smaller wave crests by those associated with the dominant waves, another manifestation of the shadowing model proposed by Wetzel.

Reconciliation of $U^{0.5}$ and U^{1} Dependences of Drag Coefficients

Beyond this implicit relationship of radar sea spikes to whitecap coverage, one can go further in suggesting a reconciliation of the U_w^1 dependence, typically observed for drag coefficient variation, vs the U_w^5 required by Wu. (U_w^5 is necessary for the $U_w^{3.75}$ dependence of whitecap coverage developed in Appendix B, which also fits our sea spike results reasonably well.) In Appendix B, we review Donelan's suggestions [19] that the total rate of energy exchange between winds and waves can be broken up into a sum of several contributions, one of which is wave breaking. Whereas the total drag coefficient measured varies linearly with U, we suggest that the wave breaking portion varies as $U^{.5}$, and this contribution is used for the radar sea spike and whitecap measurements. Thus, although Wu's derivation is based on the total wind stress, only the contribution due to wave breaking should be used in the derivation. In fact, it may be that the large spread of data points typically found in determining a drag coefficient, by empirically plotting the wind friction velocity vs wind speed, is due to the variation in the contributions of Eq. (B5) for the experimental conditions encountered.

Sea Spike RCS vs Wind Speed

Effective Mean of the Sea Spike Region vs Wind Speed

The dB-mean of the sea spike 1% intercept and the intercept of the two linear fits can be also plotted vs wind speed. Figure 9 shows these results for four of the incidence angles. For angles $>2°$, the data vary quite strongly with incidence angle, in contrast to the distributed scatter results.

Mean Sea Spike NRCS at 10 m/s

This incidence angle variation is the 10-m/s intercept values, shown plotted vs depression angle in Fig. 10(a). The sharp change is seen at 2°. Dotted circles have been drawn for the last two angles. These angles use corrections of 4 and 8 dB, the same values used earlier for the distributed scatter case. Figure 10(b) shows these same data converted to absolute cross section. At $<2°$, the RCS is nearly constant near 10 m^2, rising sharply to a peak near 2.5° and dropping precipitously with increasing angle. Finally, Fig. 10(c) shows the change in sea spike NRCS with wind speed, also determined from Fig. 9 and the other available angles.

1% Sea Spike Intercept

To give an indication, for radar design interests, of the largest sea spike to be expected as a function of wind speed, the 1% intercepts of the distributions are shown plotted vs wind speed as absolute RCS in dBm^2 in Fig. 11. The results for all 10 grazing angles are further summarized in Fig. 12 as 10-m/s values of RCS plotted vs depression angle. At $<2°$, cross sections of up to 30 m^2 (15 dBm^2) can be expected 1% of the time for 10-m/s winds. At $>2°$, the same discontinuity observed before, the maximum values grow quite markedly. Absolute cross sections of the order of 1000 m^2 are seen to occur for 6° and 7° depression angles. This is not important for shipboard operation because the ranges are just a few hundred meters, but it could be important for airborne and space-based radars.

Sea Spike Model for RCS Depression Angle Characteristics

A model is proposed to explain the above results that is a variation on one first published by Wetzel [20]. The wedge model of Lyzenga et al. [21] yields RCS that increases with increasing depression angle for horizontal (HH) polarization, rather than the falloff above 4° that we observe, and it does not describe the sharp change near 2°. Wetzel's model has difficulty with this discontinuity as well, but his model can be modified to account for it.

Figure 13 shows the geometry of three models for the plume of water spilling down the front face of a long wave, the residual body of water after a crest has broken. β is the angle that the toe of the plume makes with the surface, α is the local slope of the long wave, and θ_g is the local grazing angle. The model shown in Fig. 13(a) is that chosen by Wetzel and has a value of β equal to zero. This choice for β forces the toe to be perpendicular to the local long wave at the intersection. This assumption allows scatter to the plume from the ground plane on the near flat surface forward of the plane. This creates a corner reflector geometry, which in turn allows a variation of RCS with depression angle to occur. Scatter can occur for all incidence angles, from a surface wave parallel to the ground plane with negative incidence angle on upward. However, such a plume model is not stable because of downward gravitational forces, and one would expect a collapse. This collapse would create a toe that would be, at a minimum, perpendicular to the vertical, as shown in the second model, Fig. 13(b). For this case, $\beta = \alpha$, and a corner reflector mode is not allowed, i.e., no scatter can occur from the flat surface ahead of the plume, then off the plume, then back to the radar. (The corner reflector mode disappears for all $\beta > 0$). For the choice of β made here, with the toe perpendicular to the horizontal, scatter can occur only for positive grazing angles. Neither of these two models predicts the RCS discontinuity that we observe near 2°.

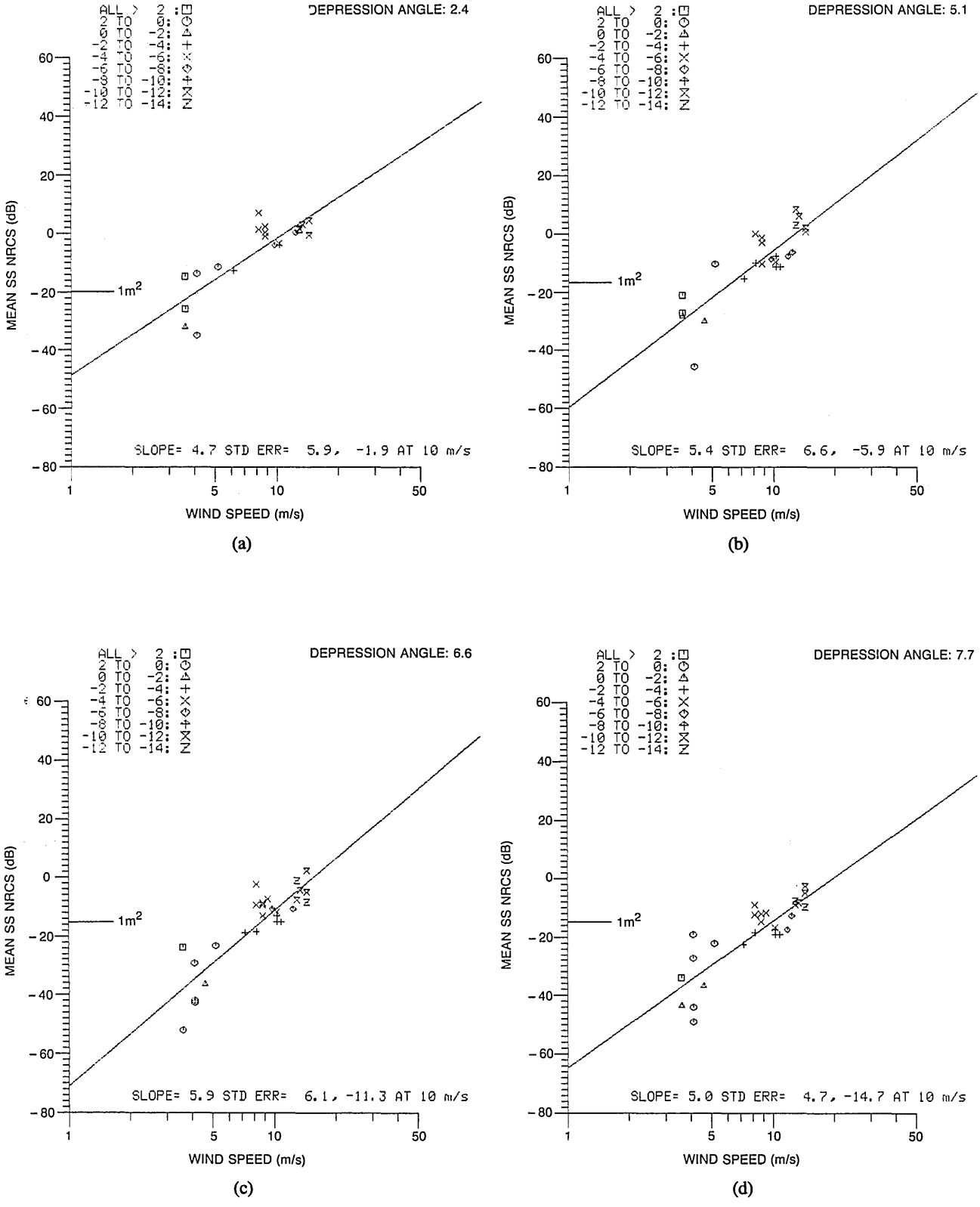

Fig. 9 — Plots of the "effective mean" of the sea spike distribution, as defined in the text, plotted vs wind speed for four radar depression angles. Note the definite dependence on depression angle.

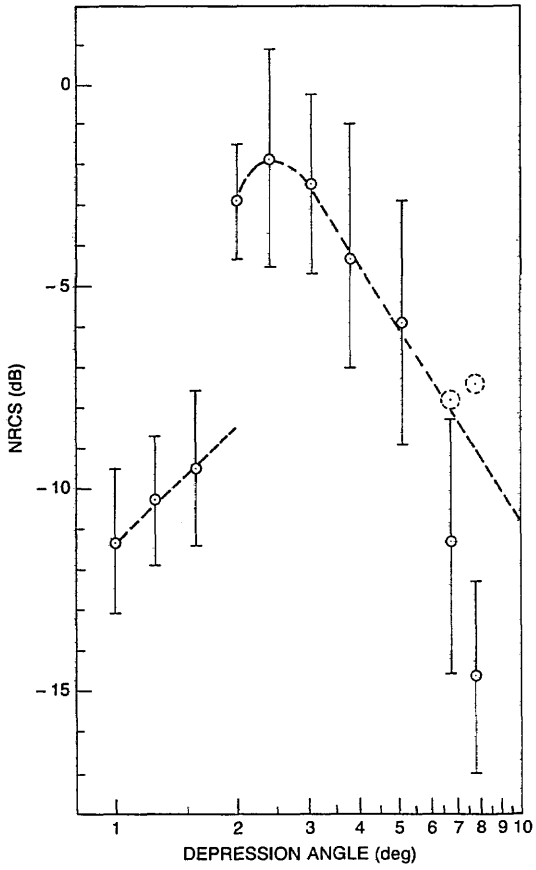

Fig. 10(a) — The sea spike mean 10-m/s intercept of Fig. 9 plotted vs radar depression angle. The last two points show the effects of the radar STC circuit, with dotted data points also drawn in, applying the correction estimated from Fig. 7(a). A sharp change is seen in the region around 2°, similar to previous parameter changes in this region.

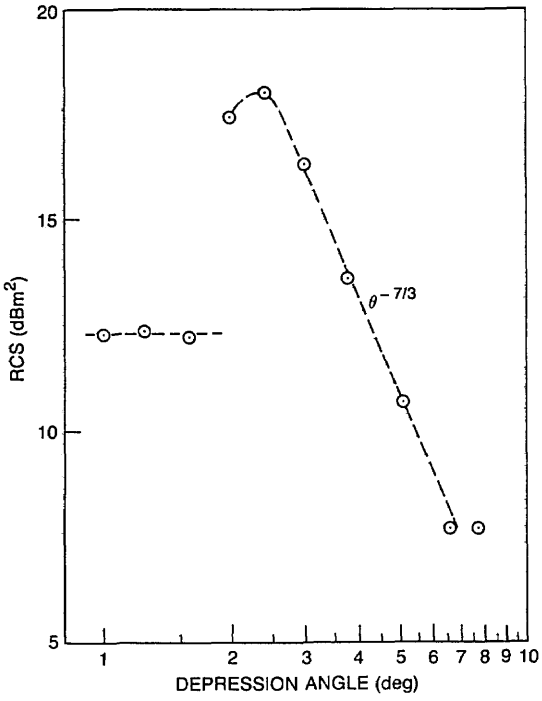

Fig. 10(b) — The sea spike total RCS value at the 10m/s intercept, results of Fig. 10(a) multiplied times the scattering cell size, plotted vs radar depression angle. The rightmost two points have been corrected and fit quite well the negative 2.33 slope with depression angle. The sharp change is still seen in the region around 2°.

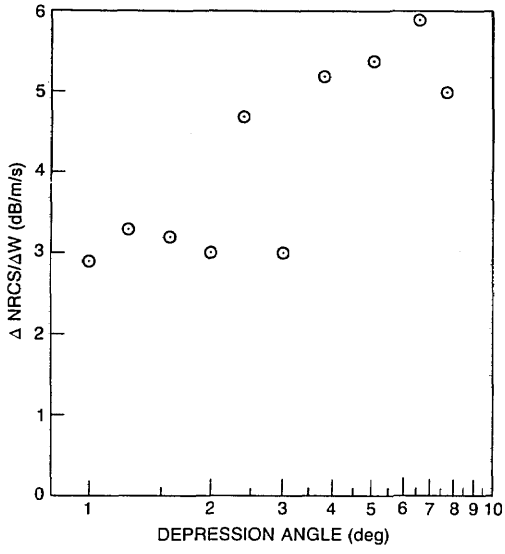

Fig. 10(c) — The change in sea spike NRCS with wind speed plotted vs depression angle

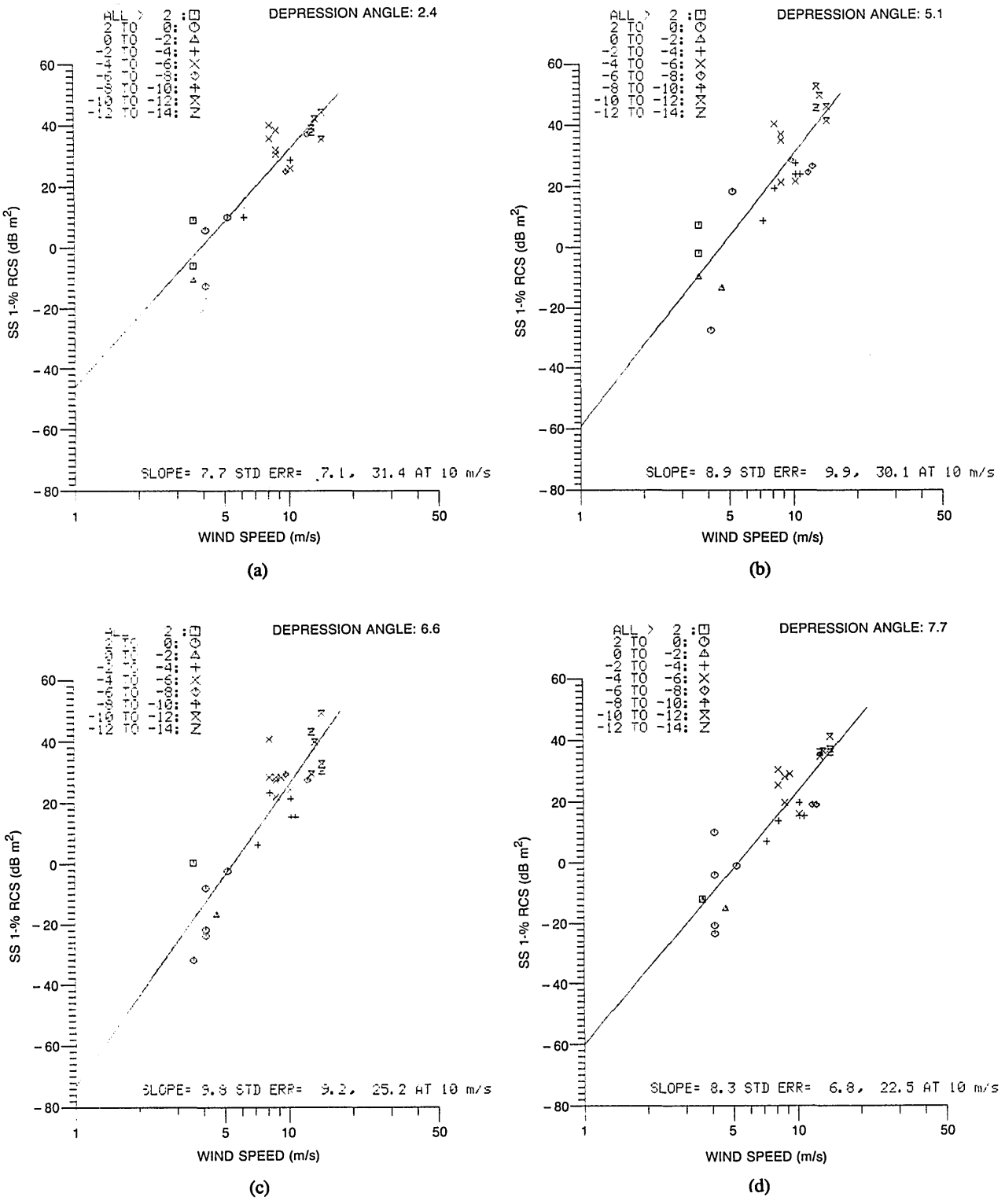

Fig. 11 — The sea spike absolute RCS at the 1% intercept of the Weibull distribution plotted vs wind speed for four of the 10 depression angles used, giving an estimate of the clutter level attained 1% of the time for detection statistics

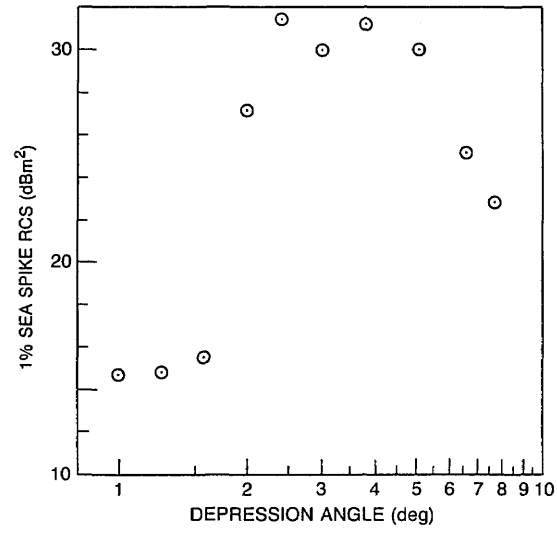

Fig. 12 — Depression angle dependence of the 1% Weibull sea spike intercept plotted for the 10 depression angles used

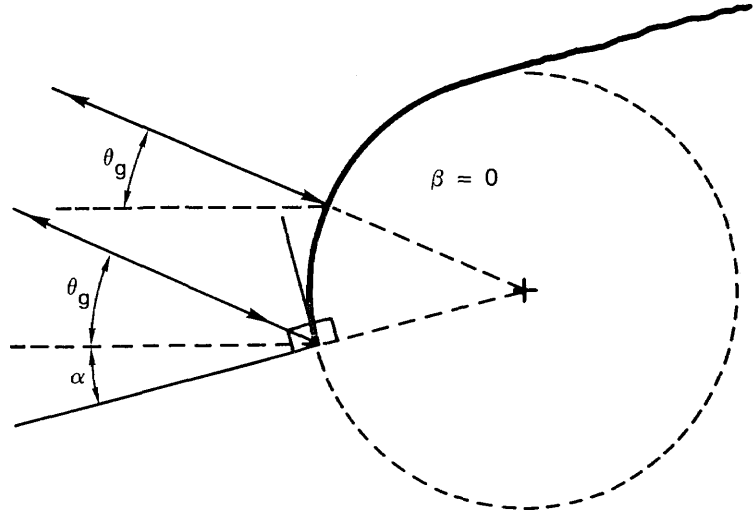

Fig. 13(a) — Breaking wave plume model of Wetzel is based upon a cylindrically shaped plume, with cylinder normal to the long wave at their intersection

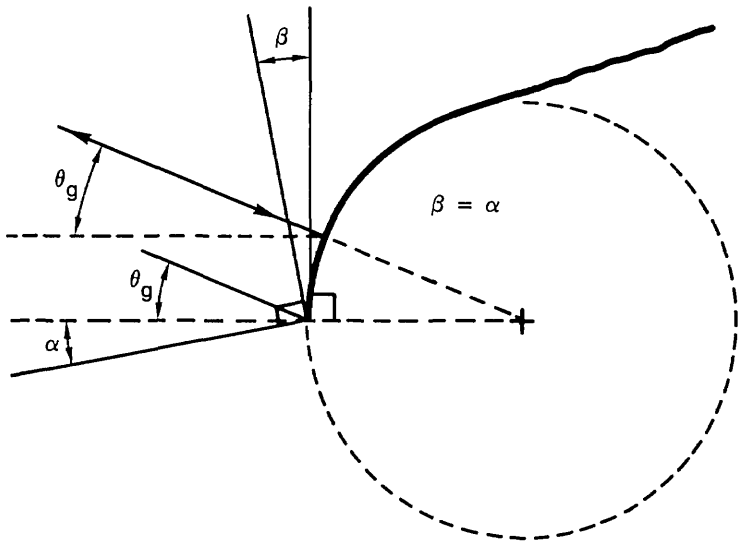

Fig. 13(b) — Modified plume model, with angle of plume intersection with ground plane perpendicular to the horizontal. This model does not allow scatter from the ground plane forward of the plume but only from the specular line along the cylinder normal to the incoming ray.

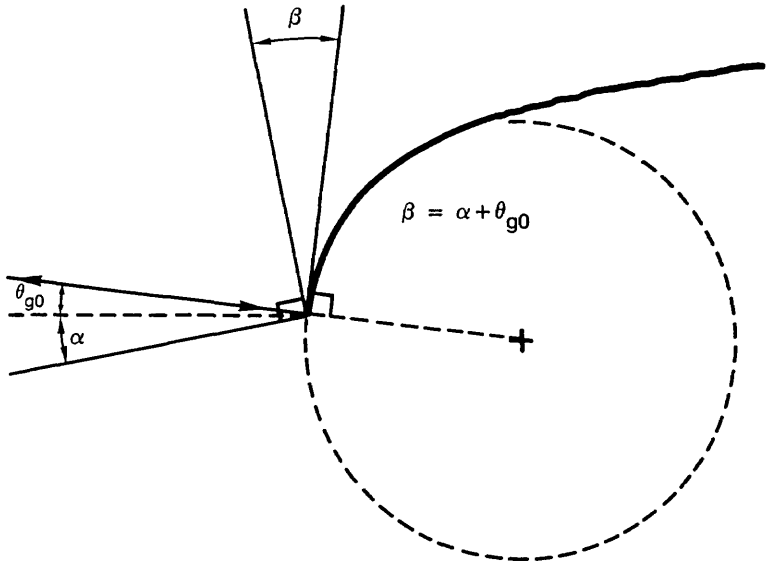

Fig. 13(c) — Modified plume model, with angle of plume intersection with ground plane at angle θ_g to the horizontal. This model allows specular scatter only from the cylinder for incidence angles greater than θ_g (2° for our data).

To predict such a discontinuity, one must assume that the toe of the plume is such that its normal is 2° positive to the horizontal, regardless of the slope of the long wave as shown in Fig. 13(c). Energy is reflected directly back to the radar only for specular reflection from the cylinder face, i.e., only for rays whose extensions pass through the center of curvature of the cylinder. Hence, for the β chosen, this occurs only for angles greater than the Θ_{g0} shown in the figure. The toe angle β must therefore be equal to the sum of the slope of the long wave at the toe α plus the minimum grazing angle θ_{g0}, which is 2° in our case.

This model now predicts a constant cross section with increasing grazing angle, since reflections from the long wave ground plane do not provide a scattering mode. The expression for such scatter from a cylinder is given by

$$\mathrm{RCS}_{\mathrm{cyl}} = kaL^2 \tag{4}$$

where a is the radius of curvature of the cylinder, k is the radar wave number, and L is the median length of a plume. If we set the RCS equal to 63 m^2 (18 dBm^2), the following combinations of a and L satisfy the equation at X-band for mean RCS values above:

a(cm)	3.2	6.4	12.8
L(m)	3.2	2.2	1.6

Using the 1000-m^2 result for the 1% intercept, the following crest lengths result:

a(cm)	3.2	6.4	12.8
L(m)	12.6	8.9	6.3

These are well within realistic surface features for a breaking plume, and all values of a satisfy assumptions of geometrical optics.

Although we have produced realistic plume features to describe the maximum RCS observed, the RCS is constant for grazing angles above θ_g with this model. However, we can account for the sharp falloff beyond 2° if we consider the radar range at which this occurs, the beamwidth of the radar, and the scale size of the plume length across the radar beam. For a 10-m crest length and a 1° azimuthal beamwidth, the crest fills the beam at a range of 573 m. For the antenna height of 24 m, this corresponds to a grazing angle of 2.4°. For shorter ranges, the crest more than fills the beam and is no longer fully illuminated, now acting as a distributed scatter in the cross range dimension. The illuminated portion is now the cross range dimension:

$$L_{\mathrm{illum}} = R\, d\phi. \tag{5}$$

In addition, we can write

$$R = H/\sin\phi \tag{6}$$

in the flat earth approximation (<5% error for angles >2.5°), and

$$R \sim H/\phi \tag{7}$$

in the small angle approximation. The expected decrease in cross section with decreasing range as the result of incomplete crest illumination is therefore given by:

$$\sigma = (2\pi a/\lambda)(R\ d\phi)^2. \tag{8}$$

When range is converted to depression angle, this becomes

$$\sigma = (2\pi a/\lambda)H^2\ d\phi^2\ \theta_{\text{dep}}^{-2} \tag{9}$$

and partially accounts for the observed angular falloff above 2.5° (−2 of the −2.33 power observed). By using either Wetzel's model or that of Lyzenga et al., increasing RCS is predicted through this region, which is in disagreement with our observations.

Finally, for grazing angles <2°, our model predicts no scatter from the plume. However, sea spikes are still present according to the observed double Weibull distribution, albeit with the discontinuous drop in RCS. Recall that these Weibull distributions are a result of sampling over the surface profile with a spatial scale smaller than the dominant wave. We have identified the first Weibull distribution with distributed scatter, presumably from portions of the wave away from the crest. The RCS distribution is determined primarily by the long wave slope distribution according to our composite model. In similar fashion, we can associate the second distribution with crest regions: with plumes providing the RCS at angles >2° and a weaker crest scattering mechanism for angles <2° (actually for all angles, but dominated by the plume model at angles >2°).

For this region, we consider the wedge model proposed by Lyzenga et al., who calculated the cross section per unit crest length-squared, RCS/L^2. This expression evaluated at 0° depression angle is −29, −23, and −17 dB for external wedge angles of 195°, 210°, and 240°, respectively. For the 10-m crest length used, these become −9, −3, and +3 dBm^2, respectively. Our mean values lie at ~12.5 dBm^2, while the 1% intercept values are at 15 dBm^2. Thus a wave crest length longer than 10 m is necessary to satisfactorily describe our results when using wedge scatter. However, the numbers used earlier as lengths are plume lengths, which can be expected to be less than the crest length that created them, according to Wetzel's development. With this caveat, we have produced a model that satisfactorily interprets all the characteristics of our observed sea spike scatter amplitudes.

Distributed-Scatter Weibull Shape Parameters

A second parameter required to fully describe the Weibull parameterization of the data, in addition to the median values, is the shape parameter B of Eq. (1). This shape parameter is the slope of the linear fit of Fig. 4. It can be expected to vary from unity, appropriate to a normal distribution of radar echo field strengths (expected to occur for very light winds), to our maximum observed values of the order of 4. This parameter that increases beyond one with larger wind speed indicates the increasing dynamic range of NRCS over which the distribution varies. Although the parameter against which the slope is plotted is the wind speed, long-wave slope increasing with wind speed is probably the cause of the growth in slope. This is expected according to the two-scale model because the local incidence angle at the scattering patch is increased on the average, which in turn contributes a larger NRCS. (This is more fully discussed in Appendix A.)

Figure 14 shows results for this parameter for one of the 10 depression angles. For very low grazing angles, the shape parameter is of the order of unity with little wind speed dependence. While the median NRCS increases with wind speed, the NRCS spread or dynamic range does not do so for low depression angles. It is possible that this is an effect of shadowing of the major portion of the

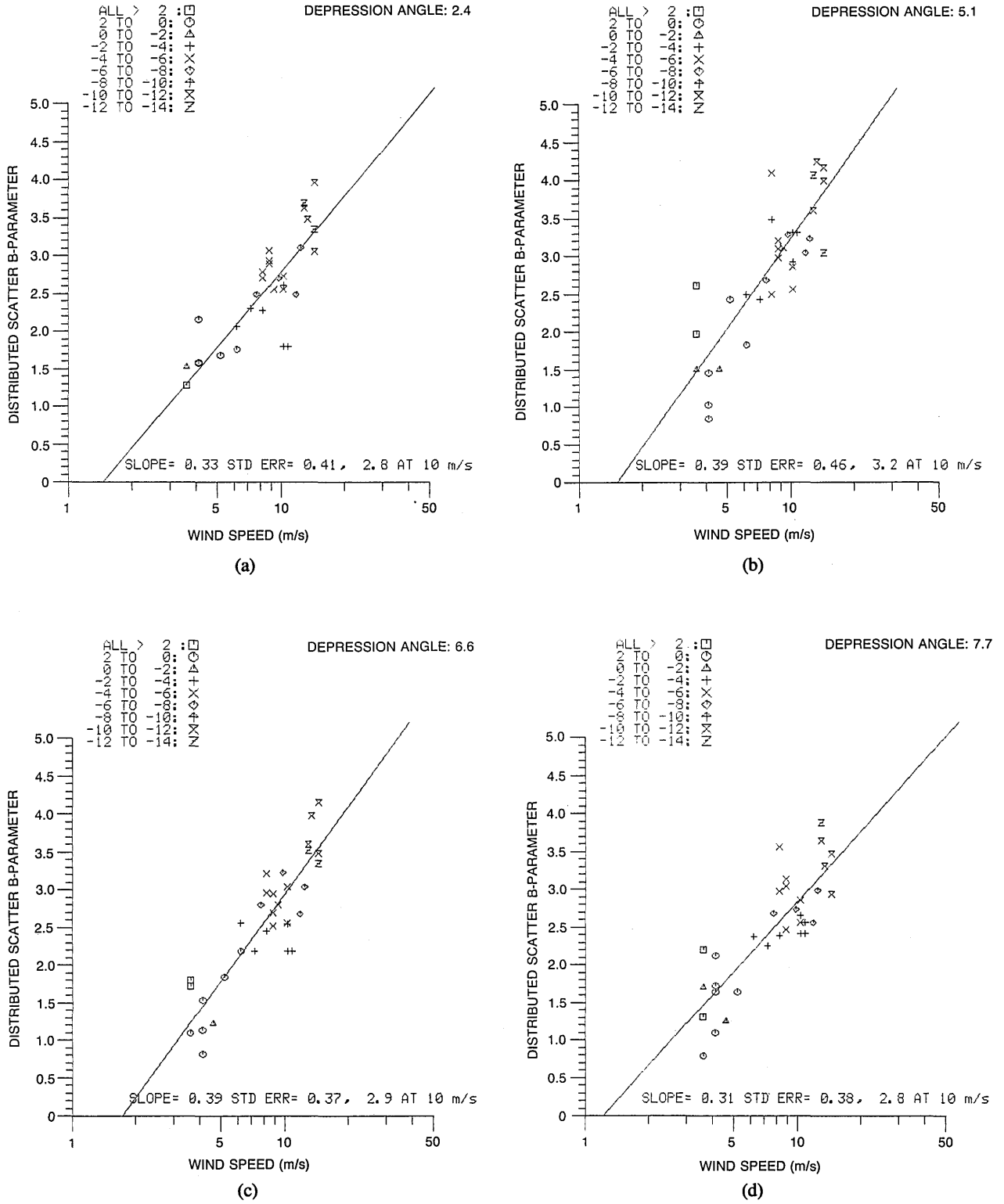

Fig. 14 — The distributed scatter Weibull shape parameter B, determined from the slope of the linear fit of Fig. 5, plotted vs wind speed for four of the 10 depression angles

sea surface by the wave crests. Less of the wave surface is illuminated, and as a result, the selection of local incidence angles is limited. These results can be summarized again by plotting their 10-m/s intercepts and slopes vs depression angle. No models currently exist to explain this behavior, since no derivation of the Weibull distribution or any other distribution from first principles has been accomplished. These results provide a first comparison set for such a model.

Figure 15(a) plots the 10 m/s intercepts vs depression angle. Again, a sharp change is seen near 2°. For all angles >2°, the value of B at 10 m/s wind speed is very nearly 3. Perhaps this is fortuitous, since the slope, or rate of increase of B with wind speed, varies with grazing angle (Fig. 15(b)). At <2°, we have fit both a linear fit as well as one that asymptotically approaches unity for small grazing angles, i.e., a Rayleigh distribution.

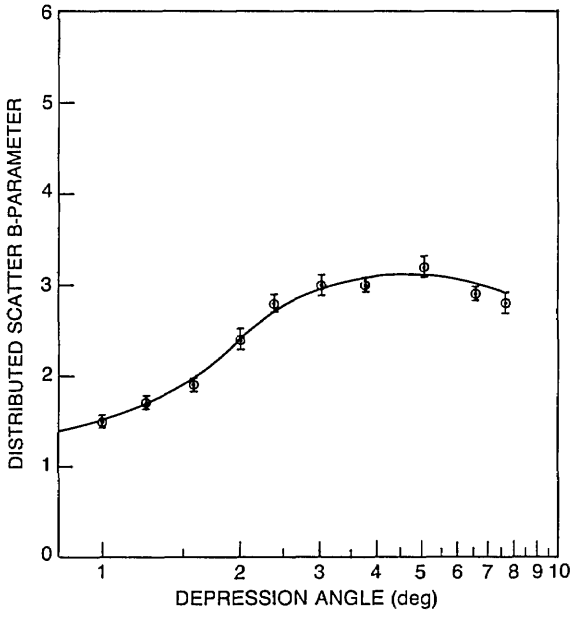

Fig. 15(a) — Intercepts at 10 m/s of the distributed scatter Weibull shape parameter plotted vs depressions angle, indicating the wind speed variation of B for each angle

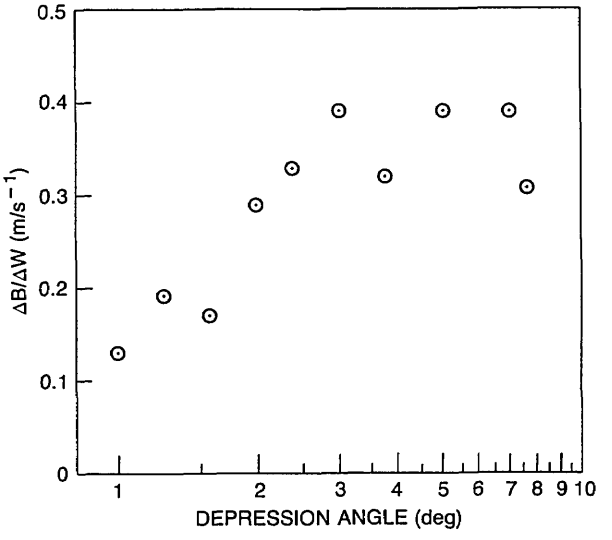

Fig. 15(b) — The change in Weibull slope parameter with wind speed plotted vs depression angle

Sea Spike Scatter Weibull Shape Parameters

Figure 16 shows an example of the data for sea spike Weibull slopes. The 10-m/s intercept of these fits to the Weibull B parameter is shown in Fig. 17(a) vs depression angle. Again, a sharp change is seen near 2°. For higher angles, the shape parameter is remarkably constant about the value 2. The slope of the Weibull parameter—wind speed variation is shown in Fig. 17(b) to complete the summary. Again, no models are available that explain this behavior.

Median NRCS vs Friction Velocity for Four Drag Coefficients

To account for the differences in atmospheric stability that occurred during the experiment, the measured air-sea temperature differences were used in four different models to provide a temperature-dependent drag coefficient. This attempt to account for atmospheric stability in air-sea interaction studies is driven by remote sensing needs, and the models that we use have all been developed in conjunction with radar experiments. These areas of research include scatterometry and synthetic aperture radar image interpretation.

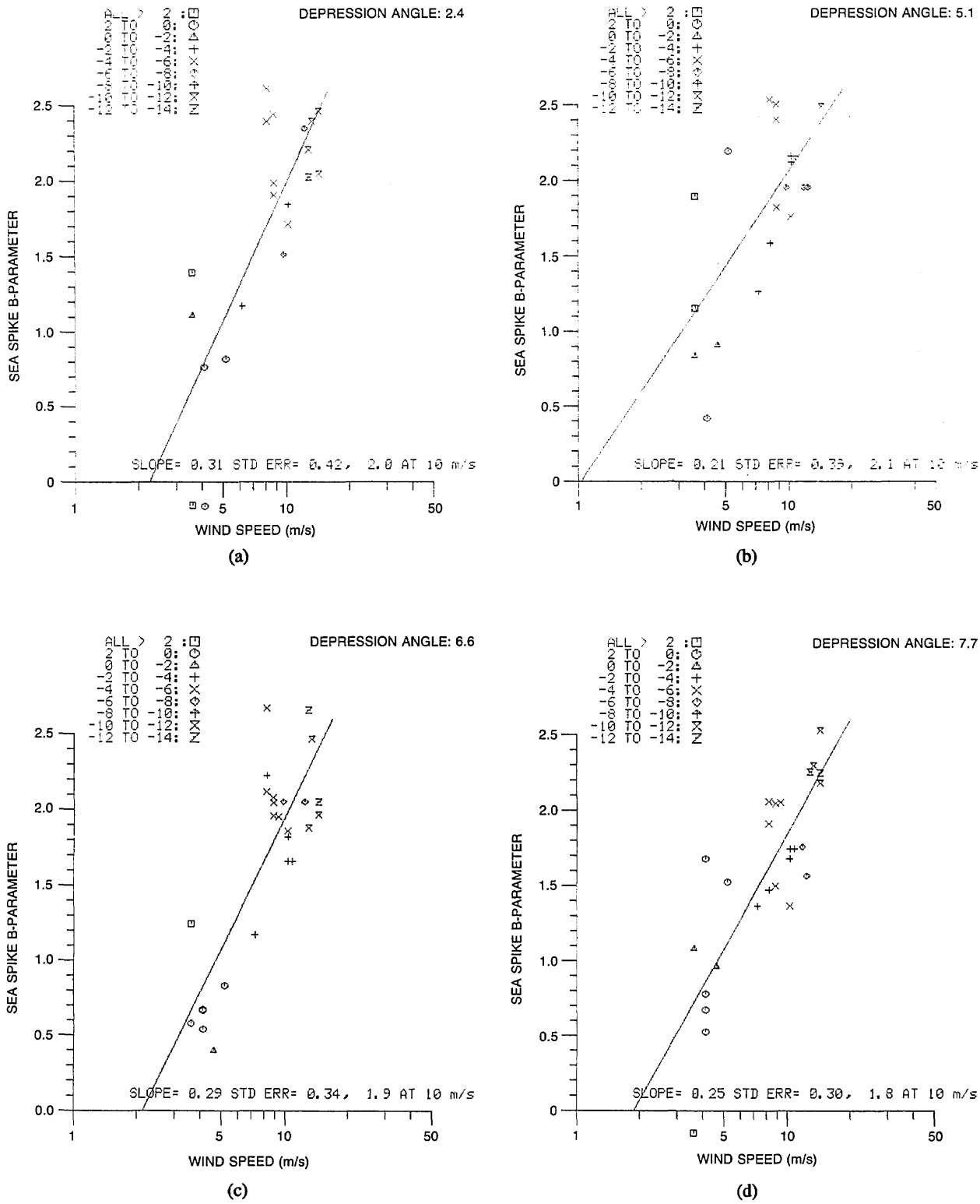

Fig. 16 — The sea spike scatter Weibull shape parameter B, determined from the slope of the sea spike linear fit of Fig. 5, plotted vs wind speed

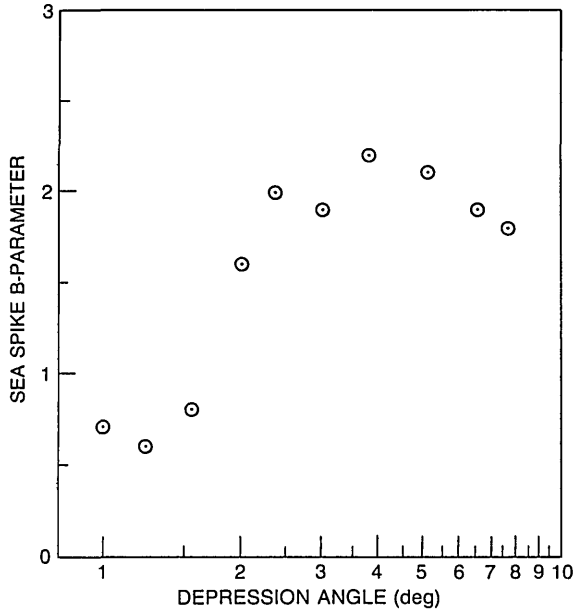

Fig. 17(a) — Intercepts at 10 m/s of the sea spike Weibull shape parameter plotted vs depression angle. At >2° the parameter is nearly constant, as was observed with the distributed scatter Weibull parameter. At <2°, the shape parameters approach one, indicating a Rayleigh distribution.

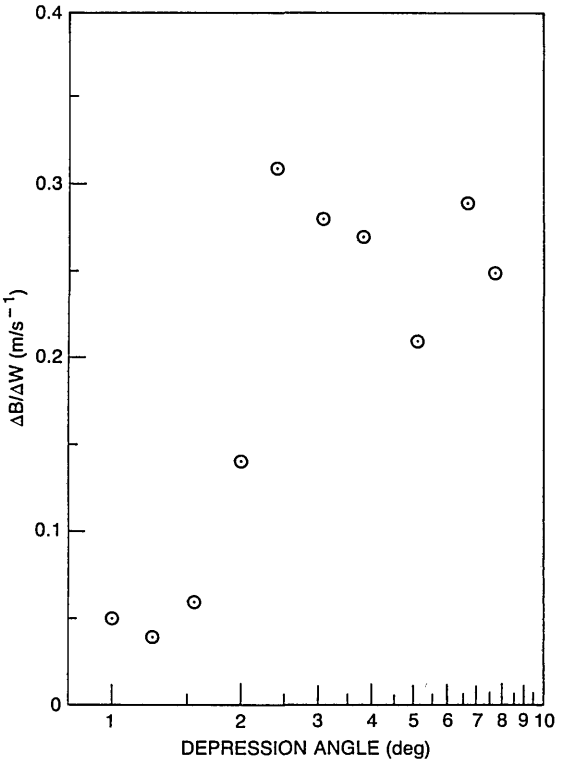

Fig. 17(b) — Slope of the sea spike Weibull shape parameter plotted vs depression angle, indicating the wind speed variation of B for each angle. These parameters are very small at <2°.

The drag coefficient allows the radar data to be parameterized against wind friction velocity. This is done by the bulk method of estimating the friction velocity that uses empirically measured drag coefficients. The bulk method assumes an equilibrium between winds and waves in terms of momentum transfer between them. For rapidly changing conditions such as at the onset or reversal of winds, more accurate techniques are required. The dissipation technique measures the fluctuations of the wind field, while the eddy correlation technique measures three orthogonal components of the wind. Because each of these techniques requires a very stable platform, they are typically not suitable for shipboard operation.

The first temperature drag coefficient used was that of Weissman et al. [22]; the second, that of Keller, Plant, and Weissman (KPW) [13] but using the $U^{0.5}$ wind speed-dependent drag coefficient of Wu discussed in Appendix B; the third, that of KPW using the drag coefficient of Large and Pond [37]; and the fourth, that of Wu [23]. Figure 18 shows results for a depression angle of 1.02. Fig. 19 shows results for a depression angle of 7.7° as plots of median NRCS vs wind friction velocity. The wind friction velocities were determined by using the measured wind speeds and Eq. (B3) of Appendix B.

The greater air-sea temperature difference increases the wind friction velocity compared to that value for zero air-sea temperature difference. Thus, for the data analyzed, the effects are only to spread the data in the horizontal plane because there is a strong correlation between wind speed and air-sea temperature difference. It is not clear whether the apparent 10-cm/s limit in the data for 7.68° is real, since there is a large spread in the data points in dB for the 2° to 0° range. The data at the

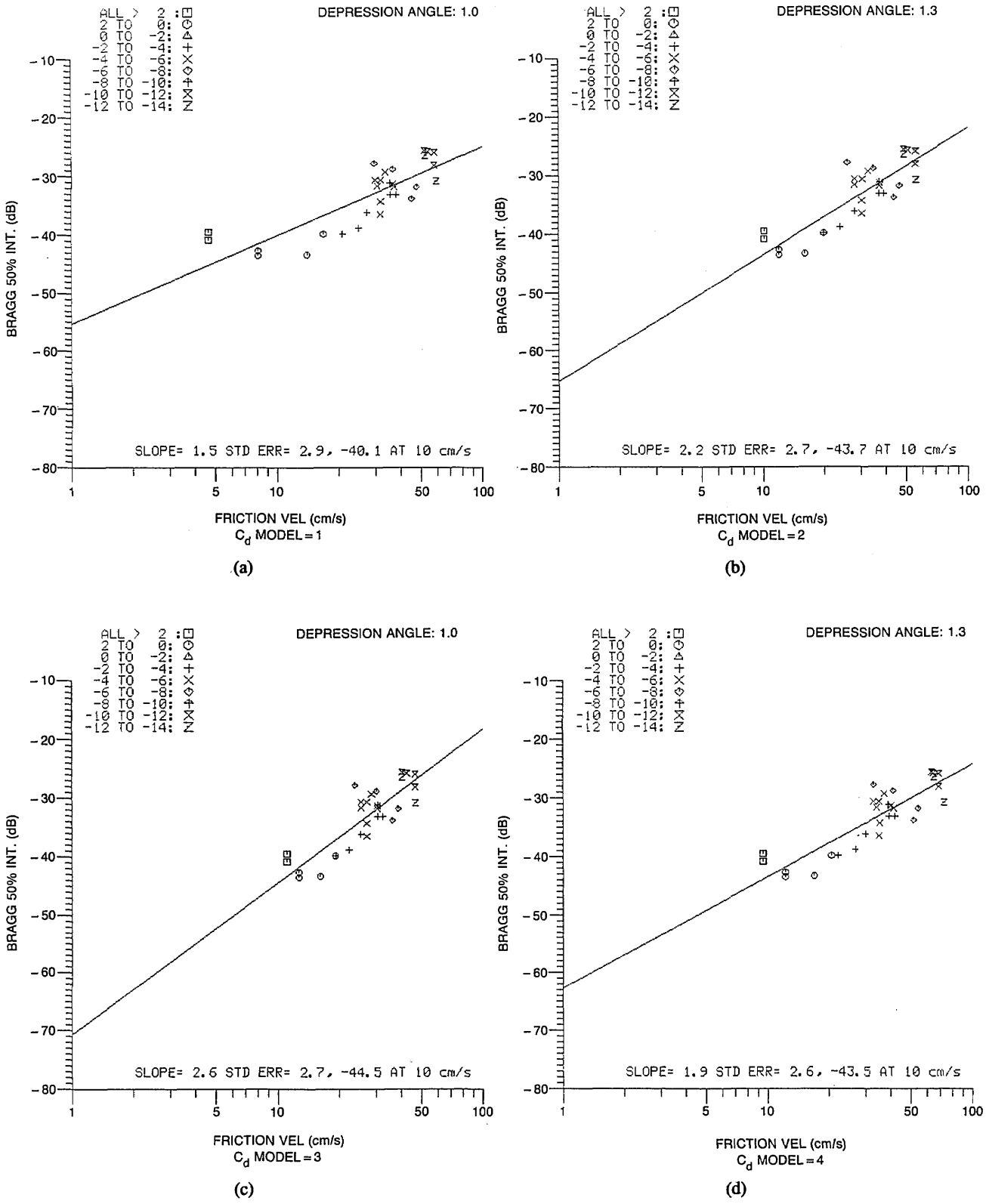

Fig. 18 — Median NRCS value at 1.02° depression angle vs wind friction velocity, for four different drag-coefficient models that account for atmospheric stability effects

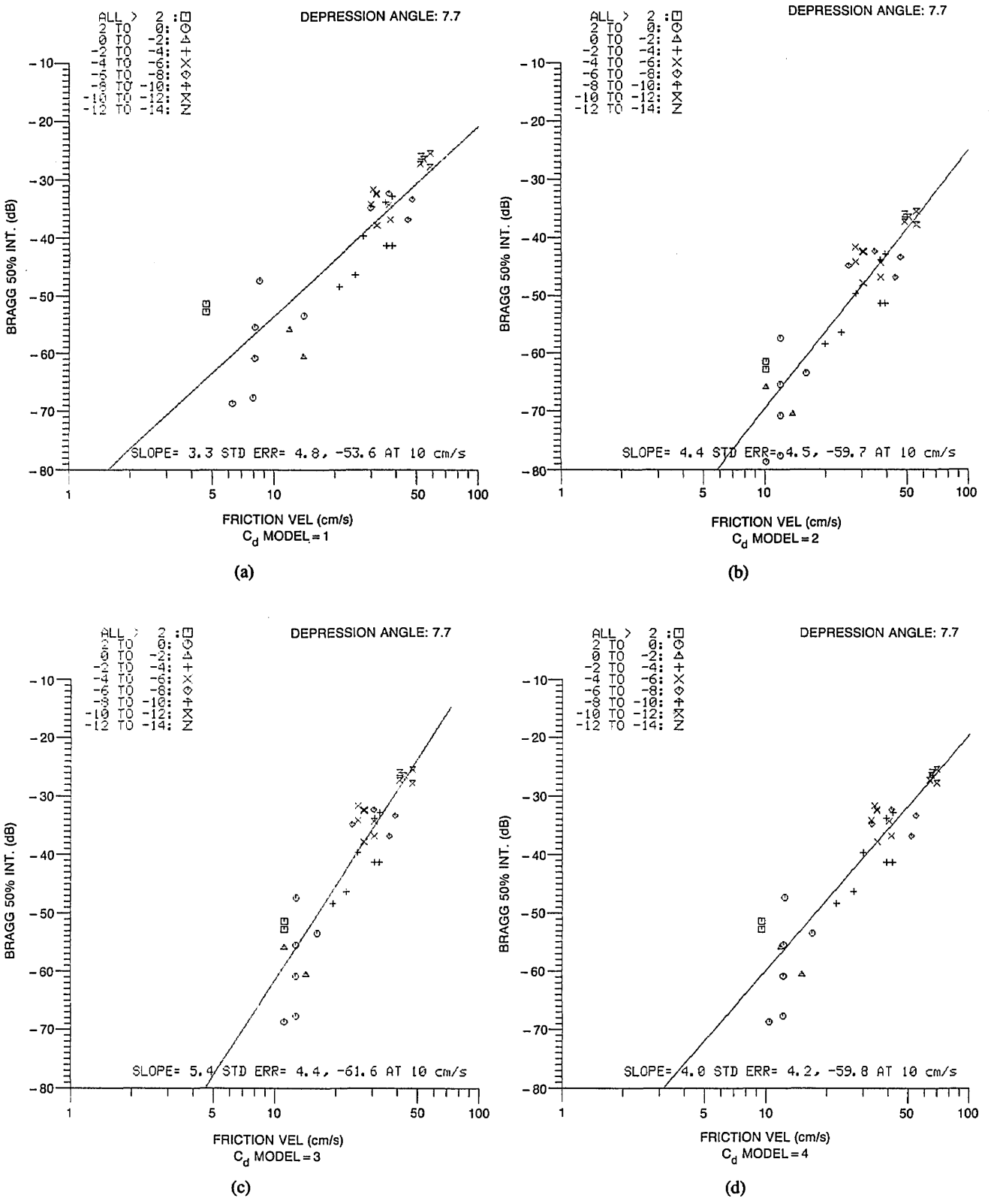

Fig. 19 — Median NRCS value at 7.68° depression angle vs wind friction velocity, for four different drag-efficient models that account for atmospheric stability effects

lowest wind speeds were collected on 10 February, after the change in wind direction. Perhaps this large spread is the results of ambient waves from the previous wind field propagating into the area.

Generally, conclusions cannot be drawn as to whether there is an air-sea temperature difference effect from these data alone. Nevertheless, they provide preliminary empirical data on which to base low grazing angle scatterometry when using a marine radar.

RELATED EXPERIMENTS

This section discusses several radar sea scatter papers that contain pertinent results. When considered as a group, results of these experiments allow inferences that can be used to form the basis of a general radar scattering model and that explain some of the features of our data. These experiments include short-pulse airborne Doppler spectrum measurements [24]; dual-polarized, short-pulse noncoherent measurements [12]; modeling of long-pulse, coherent radar Doppler spectral features as a function of sea-surface parameters [25]; dual-polarized Doppler spectra for wind-driven waves in a wave tank [26]; and comparison of horizontal HH and vertical VV polarized Doppler spectra near a coastline for relatively low wind conditions [27].

Airborne Coherent Doppler Measurements

Hicks et al. [24] conducted an airborne radar experiment using a high incidence angle, high spatial resolution, and horizontal polarization. They found that returns from regions near the crests of waves gave a larger radar return and a larger Doppler shift than returns from points along the rest of the wave. Although these results are for higher grazing angles than those considered here, they are the only deep-water results that both identify the strongest radar return with breaking features on the waves and associate a maximum Doppler shift with that region of the wave. Because the sampling scheme of our data does not identify the source of the large-NRCS region of scatter, we can rely on the observations of Hicks to identify this region with crests.

Dual-Polarized Measurements

The dual-polarized noncoherent radar sea scatter measurements of Hansen and Cavaleri [12] were nonsimultaneous but were conducted near enough in time so that the environmental conditions did not change significantly from one polarization to the next. The data were analyzed in a manner similar to that used here. Cumulative distributions were calculated for the two polarizations, and an example of their results is shown in Fig. 20. Note that the sense of the slope change is the result of the method of parameterization—plotting the percentage above a given value rather than below the value. The breaks in our data are found to occur at the same percentage and NRCS point when plotted either way. However, it was found that the break between the two distributions could be identified by curve-fitting software more effectively when plotted by using the technique in our report, particularly for low percentage occurrence of sea spikes. This is because the percentage of sea spikes are spread over a wider range in the horizontal dimension when plotted our way.

The important point to notice in this figure is that throughout the region of moderate NRCS values or Bragg region the distributions for the two polarizations have similar slopes but different 50% intercepts or medians. This consistent difference in NRCS throughout this region are what might be expected from Bragg scatter predictions for HH and VV polarizations in the low-grazing-angle regime. *In addition, if the slope of the Weibull fit is determined primarily from tilt modulation by long waves, the statistics of all VV echoes and the HH distributed scatter echoes should be determined by the statistics of the long wave slope distribution, resulting in similar Weibull slopes for both polarizations.* This picture is very much in agreement with these observations.

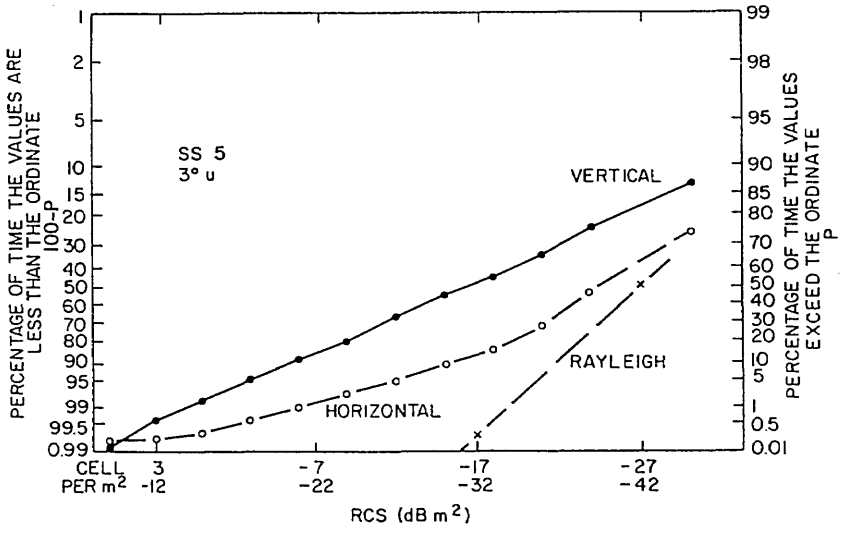

(a)

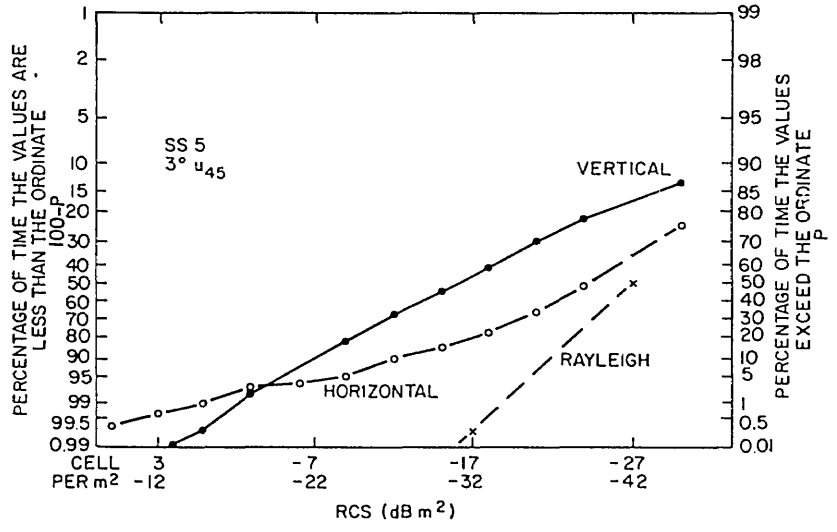

Fig. 20 — Cumulative distributions of NRCS are shown for HH and VV polarizations for X-band radar scatter collected by Hansen and Cavaleri in the Gulf of Mexico. Note the similar slopes in the moderate NRCS region of scatter, in agreement with Eq. (3).

The second point to note about the figure is that, while the HH data show a break to a second Weibull fit in the high-amplitude sea-spike region as our results do, the VV results show no such break. The VV data in the high NRCS region of the distribution continues to fit the line defined by the moderate NRCS values. Since the same ensemble of surface features are illuminated for either polarization, differences in the highest amplitude NRCS values for the two polarizations indicate a different scattering mechanism for VV polarization than for HH polarization by the surface features that are responsible for the HH sea spikes. Hansen and Caveleri found that the sea spike returns as seen on a time history of radar echo corresponded to times when wave crests passed through the scattering cell, in agreement with observations of Hicks et al. *(Thus the crests apparently scatter HH-polarized energy differently than VV polarization and behave as distributed scatterers for the VV polarization, but more coherent ones for HH polarization.)*

Doppler Spectrum Peak Shift Model

Reference 25 reanalyzes X-band data taken from a published Russian experiment [28]. In Ref. 28, Doppler shifts for HH, HV, and VV polarizations are measured, together with surface truth consisting of wind speed, rms wave height, and dominant wave period. The reanalysis found that for VV polarization the Doppler shift of the peak of the Doppler spectrum reported could be explained by a two-scale model. In this two-scale model, the scatterers' Doppler shifts were determined primarily by the orbital motions of the large waves and by the various surface currents that could arise, including Stokes currents caused by the nonsinusoidal profile that occurs for higher waves. These results are in contrast to the conclusions drawn by the Russian authors that the composite scatter model could not be used to explain their measurement results. However, they had not considered a sufficient number of effects that could contribute to the Doppler shift imposed on the radar echo by the sea surface. For light winds, where its contribution is a significant fraction of the total, it is necessary to include the phase velocity of the Bragg-resonant capillary waves to fit the data. This provides evidence for a model of Bragg scatter from wind-driven gravity capillary waves.

For HH polarization, higher scatterer velocities observed cannot be explained by orbital waves and currents, but the superimposed motions of accelerating wave crests on the large waves should be considered. The HH Doppler shifts scale linearly when plotted vs the VV shifts, with a constant multiplier of 1.4. Crest features responsible for the HH scatter are moving faster than the orbital wave velocity, as would be expected for a breaking wave. This agrees with the results of Hicks et al., in their observation of the highest Doppler shifts and largest echo power levels from the region of the wave crest for HH polarization. The types of crest motions required to satisfy the 1.4 scaling factor observed between HH and VV Doppler shifts were not considered.

Doppler Spectra

The results discussed so far are similar to the double-peaked Doppler spectra of Kwoh and Lake [26] for HH and VV data. These data cover a time containing the passage of several long paddle-driven waves with wind, produced in a wave tank. Figure 21 shows Doppler spectra for VV and HH polarizations, respectively. Both spectra exhibit double peaks, but the high and low peaks are exchanged for horizontal and vertical polarization. The magnitude of the shift of the HH peak is larger than the 1.4 scaling factor presented by Melnichuk and Chernikov. However, the wave spectra produced in a wave tank are known to be quite different from open-sea spectra, so such a comparison is probably not quantitatively meaningful. Nevertheless, the sense of the magnitude of the shift of the dominant peak in the spectrum is the same as observed in Ref. 28, indicating similar scattering mechanisms in each case. Since the spectra of Kwoh and Lake included the passage of several long waves, a Doppler shift could not be assigned to a specific portion of the wave as was done in Hicks, et al.

Open Ocean X-Band Doppler Spectra

Figure 22 shows spectra collected by Shibata et al. [27] with a C-band coherent radar and a 0.5-μs pulse for very mild winds of 4 m/s. Approach-and-recede contributions to the spectrum are observed that are unambiguous in Doppler frequency. These occur in a manner similar to those typically observed for HF radar spectra. The peaks at ± 150 Hz appear as minor contributions to the Doppler spectrum but are at ~ 1.4 times the peak of the main contribution. This agrees with the HH/VV Doppler shift ratio of Ref. 28, but the larger Doppler-shifted peak is not the dominant peak in the spectrum, as in Ref. 28. However, all results discussed so far have been for X-band radars, in which case sharp crest features may contribute a greater amplitude than for lower radar frequencies. This spectrum is also observed to be quite different from the wave tank measurements of Kwoh and Lake, which were also made at X-band.

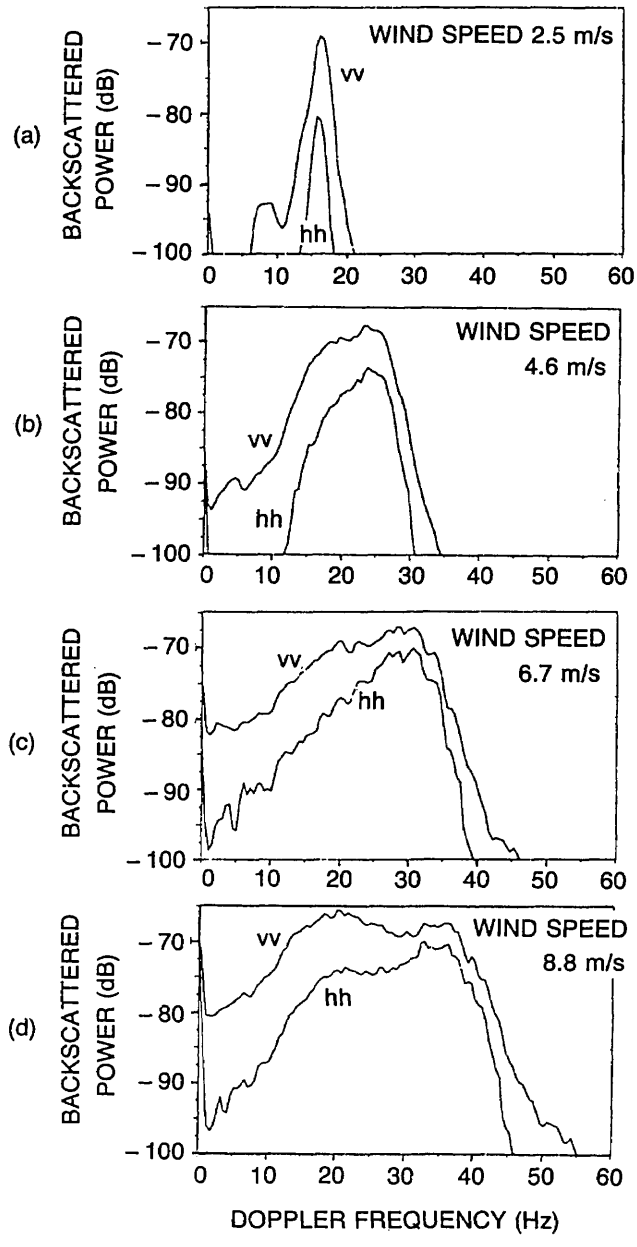

Fig. 21 — Radar Doppler spectra for scatter from waves in a wave tank for HH and VV polarizations. Note the bimodal character of each spectrum with similar location of peaks but of differing amplitudes. [Figure 3 from "The Nature of Microwave Backscattering From Water Waves," by D.S. Kwoh, et al., from *The Ocean Surface*, p. 254, published by D. Reidel Publishing Company, 1985, used by premission.]

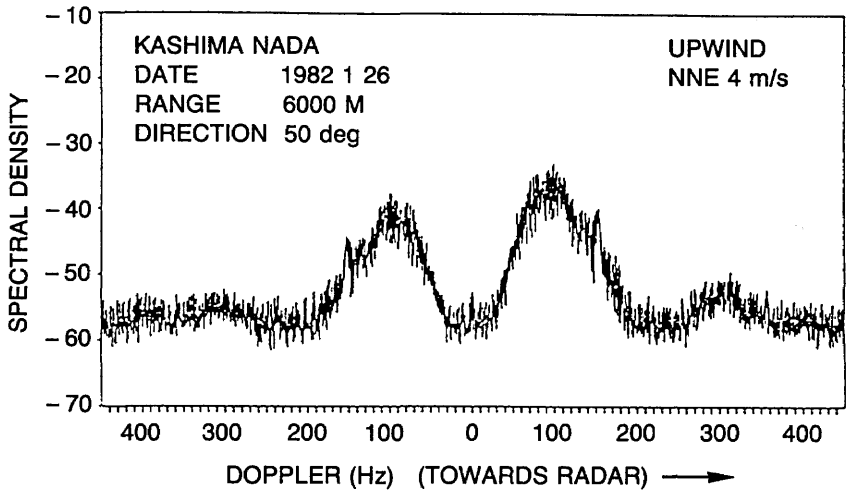

Fig. 22 — Radar Doppler spectra for scatter from open ocean waves for a C-band radar. The peaks in Doppler scale in a similar fashion as reported by Melnichuk and Chernikov at X-band for HH and VV polarization. [Figure 1 from "Doppler Spectra of Microwave Radar Echo Returned From Calm and Rough Sea Surfaces," by A. Shibata, et. al., from *The Ocean Surface*, p. 265, published by D. Reidel Publishing Company, Copywright 1985, used by premission.]

Summary of Experiments—Properties of a Doppler Shift Model

Considered as a group, these results show that:

- the sea scatter Doppler spectrum for open-ocean conditions is probably double peaked for both HH and VV polarizations;
- the ratio of the Doppler shifts is 1.4;
- the larger Doppler shifted peak (dominant for HH polarization) is associated with scatterers near the crest of the wave;
- for X-band, the largest amplitude spectral peak is the larger Doppler shifted of the pair for HH polarization, and the smaller Doppler shifted for VV polarization;
- for lower radar frequencies, the higher Doppler-shifted return may never dominate the spectrum for either HH or VV polarization because the scattering mechanism from crests at these frequencies is not as that strong as that at X-band;
- the two types of scattering mechanisms can be differentiated by statistical distributions or Doppler spectra for the two polarizations
- with such sorting, the statistics of the single-pulse returns of the high-amplitude or sea-spike fraction of all returns can be associated with the larger Doppler shift in the spectrum produced by coherently integrating the pulse samples over many long waves.

Therefore, considering Doppler spectra together with dual polarized NRCS statistics provides a preliminary model for scattering mechanisms that are in joint agreement and which together provide more information than each considered alone. These results aid in the interpretation of the results presented here as well. Although the different scattering mechanisms provide different statistics for

the two polarizations for the high spatial resolution case considered here, the transition to a Rayleigh distribution with increasing radar cell size by the central limit theorem is not expected to be easily modeled.

SUMMARY

We have reported on open ocean measurements of low grazing angle radar sea scatter made by using a shipboard marine radar. The data analysis consists of assembling cumulative distributions of NRCS values for each of several range bins from an azimuthal sector 60° wide. This sector is centered about the direction that exhibits the maximum scatter amplitude. The cumulative distributions are plotted on Rayleigh probability paper on which Weibull distributions plot as straight lines, the Rayleigh distribution being one of the family of Weibull distributions.

The distributions exhibit linear features in the high and middle regions of the NRCS-percentage plane, while the lowest amplitude region round off to a minimum NRCS value. This latter rounded contribution is attributed to a partial contribution of noise values that are the result of samples collected from shadowed regions of the surface and/or samples from regions that exhibit NRCS values that fall below the noise level of the receiver. The two regions showing linear behavior are attributed to two different scattering mechanisms. From the behavior of the data with increasing range, these are shown to be due to a distributed scattering mechanism for the midlevel NRCS region of scatter and localized discrete scattering surface features for the highest level region of NRCS values. Current models for scatter suggest that these two mechanisms are Bragg and sea spike scattering mechanisms, respectively.

The characterization of the two distributions with environmental parameters is accomplished by determining parameters of the Weibull linear fits to the data and plotting these vs wind speed measured aboard the ship. The parameters used are the median value and slope of the Bragg-related Weibull distribution, and "effective mean" and slope of the sea spike-related Weibull distribution. The intercept of the two Weibull linear fits has also been calculated, and the NRCS and percentage value coordinates of this point are stored. The Bragg median value typically corresponds to the median value of the entire distribution as well.

The results of the correlation of radar parameters against environmental parameters is summarized as follows:

- The median NRCS of the distributed scatter contribution to the cumulative distribution can be fit as exponentially varying with wind speed, with a power ranging from 2 to 5.75 as the depression angle varies from 1° to 7.7°.

- The median NRCS varies very little with increasing radar depression angle, in agreement with a composite scatter model incorporating Bragg scatter in this region.

- The percentage occurrence of sea spikes can be roughly fitted by an exponential wind speed asymptote satisfying

$$SS\% = 70\% * (U / U_{10m/s})^{3.75},$$

the power law dependence similar to that observed for whitecap coverage of the ocean surface. For the higher winds in these observations, the data fall below the asymptote, caused

either by the seas not being fully developed for lack of fetch or time or because the linear curve is an incorrect form in this region.

- For all depression angles $>2°$, the Weibull shape parameter B for the distributed scatter component at 10 m/s wind speed is ~ 3, increasing with wind speed.

- For all depression angles $>2.5°$, the Weibull shape parameter B for the sea-spike scatter component at 10-m/s wind speed is ~ 2, also increasing with wind speed.

- For depression angles $<2°$, the Weibull shape parameters appear to approach unity for the distributed scatter component (Rayleigh distribution of radar echo field strength) and 0.75 for the sea-spike component.

- The weak variation of distributed scatter NRCS with grazing angle is in agreement with a Bragg scatter mechanism if tilt modulation is assumed and by using local long wave slope of the order of 16° to 20° on the leeward slope of the wave. However, the levels are much too high to be explained by horizontally polarized Bragg scatter composite model.

- The variation of mean sea-spike absolute RCS has the wrong sense with depression angle to be described by Bragg scatter, since it is negative for increasing depression angle, varying as 0 to 2.33 for depression angles $>2°$. At this point, shadowing effects modify the distribution of NRCS with decreasing depression angle and affect the calculation of the mean RCS. This variation with depression angle is in the opposite sense of that predicted by either the wedge model or Wetzel's spilling plume model.

- The variation of distributed-scatter NRCS with wind-friction velocity, which attempts to account for atmospheric stability effects by an air-sea temperature-dependent drag coefficient, shows too much scatter to differentiate between three current temperature-dependent models.

Some statements can be made about the errors involved in the data analysis. The accuracy with which the wind speed can be measured is a topic of concern, and several errors can occur. These are primarily caused by the effects of flow distortion of the wind around the ship's superstructure, enhanced for cases when the ship is not traveling into the wind. Recent model studies by Blanc [29] have shown that flow distortion can produce errors as large as 40%, depending on where the anemometer is located relative to the superstructure. Since the relative wind direction was not available, this effect could not be minimized. Future experiments are planned in which the relative wind vector will be measured, i.e., the ship's heading as well as wind direction.

Current models for high grazing angle scatterometry suggest that the radar sea echo may be more closely related to the wind stress or wind-friction velocity. This is most accurately determined by measuring the fluctuations in the wind with in situ sensors and is independent of the absolute values of the wind speed. We have used an empirical bulk method of determining wind friction velocity in this work, based on measurement of the wind speed. While wind fluctuation measurements are also affected by ship flow distortion, the errors can be minimized by sorting according to wind direction relative to the ship heading, and these experiments are also planned. They will use dissipation techniques to measure wind stress.

The errors in the absolute measure of radar cross section are somewhat uncertain, since the calibration sphere shows some fluctuations, presumably caused by multipath from the sea surface. However, preliminary processing of a second experiment using S- and X-band radars on the same ship

show differences of <2 dB for mild winds when the Bragg scatter model is expected to hold. In addition, these results fit the straight lines determined from the data reported here quite well. Thus, it is estimated that the radar cross sections are accurate to within less than a few dB. In future experiments, upwind-downwind and upwind-crosswind results will be available as well.

ACKNOWLEDGMENTS

The author gratefully acknowledges the contributions made during this work. Melvin Lehman provided much general knowledge in the area of interfacing to the radar and calibrations. Pete Hansen designed an interface box that allowed combining antenna pointing angle and video signal onto a common analog data signal for digital conversion to allow determination of pointing direction for each pulse. Donna Donovan designed the software for the automatic collection and storage of data, in addition to preliminary processing programs. Rod MacLean completed the analysis software. Several people were responsible for tedious processing of a significant amount of radar data through several stages: Ann Ludden, Sandeep Das, and John Sawyer. Lastly, I acknowledge the review and suggestions by Lew Wetzel that greatly improved the report.

REFERENCES

1. B.L. Lewis and I.D. Olin, "Some Recent Observations of Sea Spikes," IEE Conf. Pub. 144, p. 115, 1975.

2. B.L. Lewis, J.P Hansen, I.D. Olin, and V. Cavaleri, "High Resolution Radar Scattering Characteristics of a Disturbed Sea Surface and Floating Debris," NRL Report 8131, July 1977.

3. B.L. Lewis and I.D. Olin, "Experimental Study and Theoretical Model of High-Resolution Radar Backscatter from the Sea," *Radio Sci.* **15** 815-828, (1980).

4. I.D. Olin, "Amplitude and Temporal Statistics of Sea Spike Clutter," IEE Conf. Pub. 216, pp. 198-202, 1982.

5. I.R. Young, W. Rosenthal, and F. Ziemer, A 3-Dimensional Analysis of Marine Radar Images for the Determination of Ocean Wave Directionality and Surface Currents, *J. Geophys. Res.*, **90**(C1), 1049-1059 (1985).

6. D.B. Trizna and D. E. Porter, "Measurement of Waveheight and Dominant Wave Period using a Coherent Shipboard Radar," Oceans 84, Marine Technology Society, Washington, D.C., 1984 pp. 134-137.

7. D.C. Scheler, "Radar Detection in Weibull Clutter," *IEEE Trans.*, **AES-12**, 736-743 (1976).

8. J. Clarke and R.S. Peter, "The Effect of Pulse Length Changes on Weibull clutter," Royal Radar Establishment Memorandum 3033, 1976.

9. F.A. Fay, J. Clarke, and R.S. Peter, "Weibull Distribution Applied to Sea Clutter," IEE Conf Pub. 155, pp. 101-104, 1977.

10. R.S. Burington and D.C. May, *Handbook of Probability and Statistics with Tables,* 2nd ed. (McGraw Hill, New York, 1970).

11. A.I. Kalmykov and V. V. Pustovoytenko, "On Polarization Features of Radio Signals Scattered from the Sea Surface at Small Grazing Angles. *J. Geophys. Res.*, **8**, 1960-1964 (1976).

12. J.P. Hansen, and V. F. Cavaleri, "High Resolution Radar Sea Scatter, Experimental Observations and Discriminants," NRL Report 8557, Mar. 1982.

13. W.C. Keller, W. J. Plant, and D. E. Weissman, "The dependence of X-band Microwave Sea Return on Atmospheric Stability and Sea State," *J. Geophys. Res.*, **90** (C1), 1019-1029, (1985).

14. Sittrop, H., "Characteristics of Clutter and Targets at X- and Ku-band," AGARD 31st Tech. Meeting, Conf. Proc. 197, 1976.

15. N.E. Huang, S.R. Long, and L.F. Bliven, "On the Importance of Significant Slope in Empirical Wave Studies," *J. Phys. Oceanogr.*, **10**, 569-573 (1981).

16. L.B. Wetzel, A Model for Sea Backscatter Intermittency at Extreme Grazing Angles," *Radio Sci.*, **12** (5) 749-756 (1977).

17. M.W. Long, *Radar Reflectivity of Land and Sea,* (Heath & Co., Lexington, Mass., 1975).

18. Jin Wu, "Oceanic Whitecaps and Sea State," *J. Phys. Oceanog.*, **9**, 1064-1068 (1979).

19. M.A. Donelan, "Whitecaps and Momentum Transfer, in *Turbulent Fluxes through the Sea Surface, Wave Dynamics, and Prediction,* A. Faivre and K. Hasselmann, eds. (Plenum Press, New York, 1978) pp. 273-287.

20. L.B Wetzel, "On Microwave Scattering by Breaking Waves," in *Wave Dynamics and Radio Probing of the Ocean Surface,* O.M. Phillips and K. Hasselmann, eds., (Plenum Press, 1986) pp. 273-284.

21. D.R. Lyzenga, A.L. Maffett, and R.A. Shuchman, "The Contribution of Wedge Scattering to the Radar Cross Section of the Ocean Surface," *IEEE Trans. Geosci. Remote Sensing*, **GE-21**, 502-505 (1983).

22. D.E. Weissman, T.W. Thompson, and R. Legickis, "Modulation of the Sea Surface Radar Cross Section by Surface Stress: Wind Speed and Temperature Effects across the Gulf Stream," *J. Geophys. Res.* **85**, 5032-5042 (1980).

23. Jin Wu, "Stability Parameters and Wind-Stress Coefficients under Various Atmospheric Conditions, *J. Atm. and Oceanic Tech.*, **3** (2) 333-339 (1986).

24. B. L. Hicks, N. Knable, J. J. Kovaly, G. S. Newell, J.P. Ruina, and C. W. Sherwin, "The Spectrum of X-band Radiation Backscattered from the Sea Surface," *J. Geophys. Res.*, **65**, 825-837 (1960).

25. D.B. Trizna, A Model for Doppler Peak Spectral Shift for Low Grazing Angle Sea scatter," *IEEE J. Oceanic Eng.*, **OE-10**, 368-375 (1985).

26. Kwoh, D.S.W., and B.M Lake, "The Nature of Microwave Backscattering from Water Waves," in *The Ocean Surface, Wave Breaking, Turbulent Mixing and Radio Probing*, Y. Toba and H. Mitsuyasu, eds. (D. Reidel, Boston, 1985) pp. 249-256.

27. Shibata, A., T. Uji, I. Isozaki, K. Nakamore, J. Awaka, Doppler Spectra of Microwave Radar Echo Returned from Calm and Rough Sea Surfaces in *The Ocean Surface, Wave Breaking, Turbulent Mixing and Radio Probing*, Y. Toba and H. Mitsuyasu, eds. (D. Reidel, Boston, 1985) pp. 263-268.

28. Y.U. Melnichuk and A.A. Chernikov, "Spectra of Radar Signals from Sea Surface for Different Polarizations," *Isvestia, Atmos. Oceanic Phys.* **7**, 17-24 (1971).

29. T. Blanc, "Superstructure Low Distortion Correction for Wind Speed and Directions Measurements Made from Tarawa Class (LHA1-LHA5) Ships," NRL Report 9005, Oct. 1986.

Appendix A

LOW GRAZING ANGLE SEA SCATTER BACKGROUND

COMPLEXITIES ENCOUNTERED FOR SHALLOW GRAZING ANGLES

In this section we discuss the difficulties encountered for low grazing angle sea scatter, as compared to that for higher illumination angles appropriate to aircraft or satellite radars. Assume that a distributed scattering mechanism is operative in the low grazing angle case, such as Bragg scatter, since it appears to give a qualitatively correct description for higher angles. The behavior predicted by this mechanism for low grazing conditions is examined. In addition, two other items peculiar to low grazing angles arise: shadowing of the surface by crests of the steepest waves and the occurrence of radar sea spikes. These latter are deterministically associated with breaking or sharply crested features on the surface and are expected to be the result of a localized scattering mechanism. Each of these is now examined in some detail.

Bragg Scatter

At very low grazing angles, say $<10°$, the variation of the normalized radar cross section (NRCS) with depression angle predicted by the Bragg scatter model is more severe than for moderate angles, roughly between 30° and 60°. This behavior is shown in Fig. A1 (from Valenzuela [A1]) for vertical polarization. For very high depression angles, between 60° and 90°, specular reflections from small-scale facets on the long-wave features of the ocean surface dominate the scatter. For smaller depression angles, in the 60° region and lower, Bragg scatter is predicted as dominating the radar return. Returns expected from sea spikes are not shown here. The Bragg scattering mechanism is caused by resonant-type reflections from ocean wave components with wavelength satisfying the Bragg relation between the radar wavenumber k and the ocean wavenumber K:

$$K = 2k \sin\theta \tag{A1}$$

where θ is the incidence angle as measured from nadir. It was first suggested as a mechanism for radar scatter by Crombie, who was studying sea scatter at HF frequencies [A2]. For our purposes, the Bragg model is sufficient to illustrate the effects of the rapid decrease of radar echo with decreasing depression angles.

The NRCS of the sea surface for Bragg scatter [A3] is given by

$$\sigma^0 = 4\pi k^4 \cos^4\theta \mid G_{ij} \mid^2 W(2k \sin\theta, 0), \tag{A2}$$

where

$$G_{HH} = (\epsilon - 1) / [\cos\theta + (\epsilon - \sin^2\theta)^{1/2}]^2, \tag{A3}$$

$$G_{VV} = \frac{(\epsilon - 1)\,[\epsilon(1 + \sin^2\theta) - \sin^2\theta]}{[\epsilon \cos\theta + (\epsilon - \sin^2\theta)^{12}]^2}, \tag{A4}$$

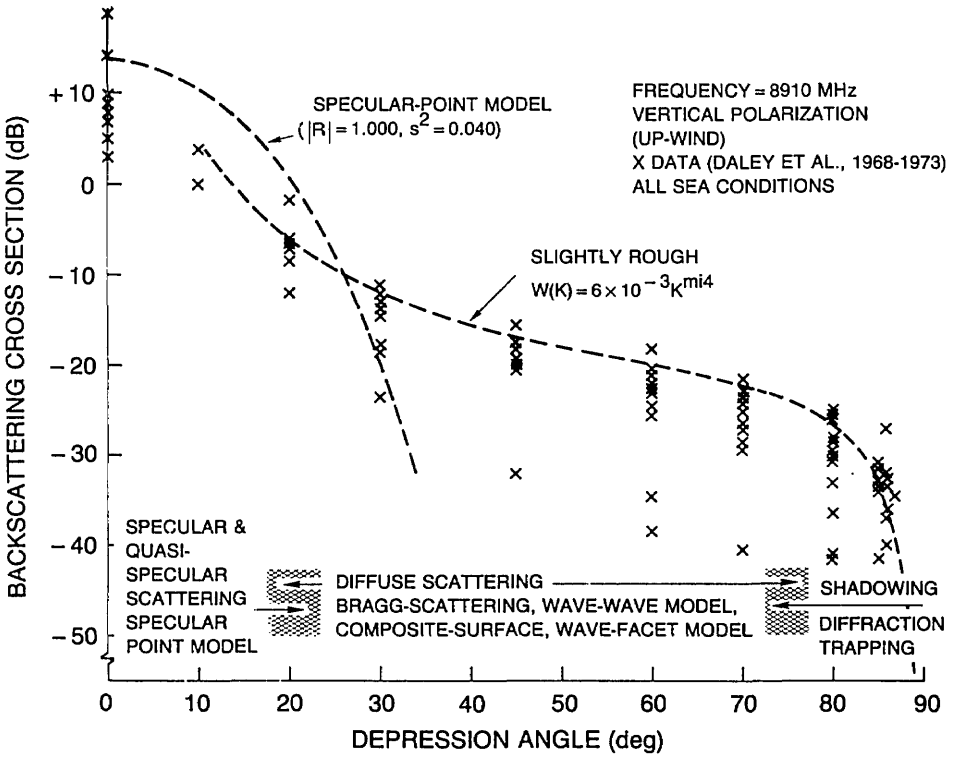

Fig. A1 — The Bragg scatter model is shown as the region from 80° downward to grazing, in this plot showing the variation of NRCS with local incidence angle at the surface

and where $W(k_x,k_y)$ is the two-dimensional Cartesian ocean wave number spectral density. The strong variation of Eq. (B2) at small depression angles is also shown in Fig. A1. However, rather than the depression angle as measured at the radar, the local incidence angle at the point of scattering is important. For the open ocean and at microwave frequencies, shallow local grazing angles are encountered infrequently because of the tilting of small-scale structure by long waves. Such tilting will modify the NRCS observed at shallow grazing, and this predicted behavior is discussed in the composite model section.

Shadowing of Radar Energy by Steep Wave Crests

Regarding shadowing, radar energy propagating just over the tops of the highest waves will not illuminate the ocean surface just behind the wave crests for very small depression angles. This effect is shown in Fig. A2(a-c) for three different depression angles and illumination in the upwind direction. In the first case, appropriate to illumination from an aircraft or satellite radar, the entire surface is illuminated and no shadowing is encountered. In the second example, some shadowing of the troughs of the waves occurs, but virtually all wave crests on the forward face of the long wave are illuminated. In the last example, only the highest wave crests are illuminated, these being associated with the dominant waves of the ocean wave spectrum. The transition from case two to case three will be important for later considerations. The shaded region in each of the figures is defined as the shadowed region, and radar samples at the time delays associated with these regions would result in samples of receiver noise, since no echo from the surface occurs. For a long-pulse radar operating at low grazing angles, such shadowing prevents one from relating the NRCS to the roughness of the ocean because the percentage of the ocean surface illuminated is uncertain.

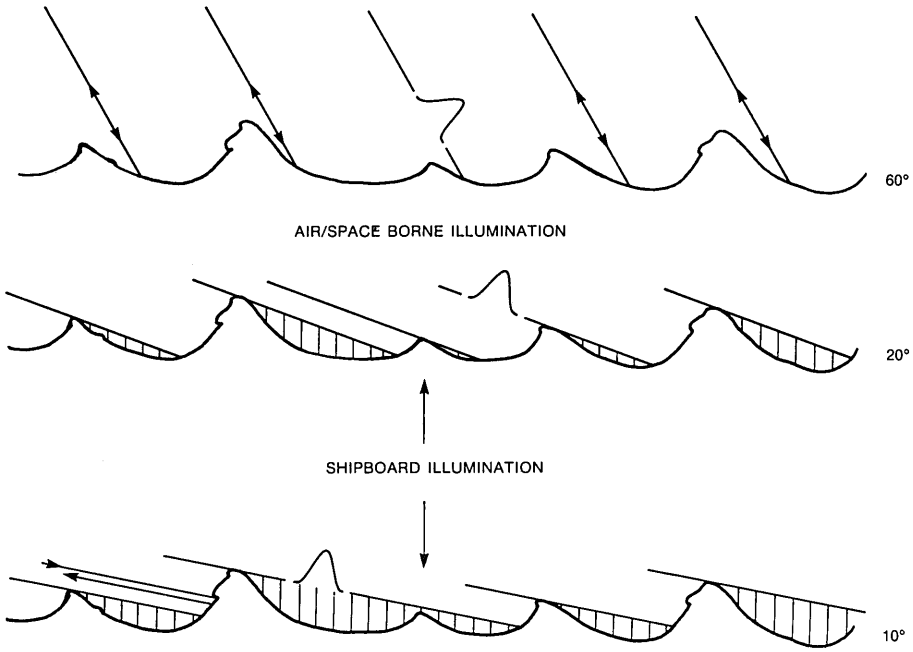

Fig. A2 — (a) The geometry for moderate grazing angles and a high-resolution radar. Small-scale, wind-driven, and surface turbulence fine structure varies across the long wave, producing a distributed scatter source. Surface features due to incipient breaking and wave crests provide localized scatterers, which are not important at moderate to high angles. (b) The same surface is shown illuminated at a moderately low grazing angle. The surface below the hatched region is shadowed by a wave crest and produces samples of the receiver noise. At this angle, the crests and leeward-face breaking features are responsible for sea spike returns, none of which are shadowed for this grazing angle. (c) The same surface is shown illuminated for a very low grazing angle. Now the smaller wave crests on the leeward face are shadowed, in addition to a large portion of the distributed scatter region, and the surface behaves in a manner similar to Wetzel's scattering model [20].

Sea Spikes

Radar sea spikes have been defined by their behavior in a sea echo time series as the highest amplitude returns whose temporal behavior appears to have a very small variation over an extended period of time. However, as they are the largest echo of the time series, they have also been shown to have a different statistical characterization when displayed on a cumulative distribution of RCS by Hansen and Cavaleri [A4] and by Olin [A5]. They were shown to be deterministically associated with crest and breaking features on the surface [A4], and the scattering mechanism describing them would have to be a localized one. Two models exist in the literature, the spilling breaker model by Wetzel [20], and any one of many wedge models, the most recent that of Lyzenga et al. [A6]. In this report we have suggested a modified version of Wetzel's to explain an anomoly in much of the data at 2° grazing angle.

THE COMPOSITE SCATTER MODEL FOR SHALLOW GRAZING ANGLES

For cases when waves much longer than the Bragg scatter wavelength are present along with the small-scale structure, such as swell in the open ocean or a paddle-generated wave in a wave tank experiment, the composite or two-scale model is necessary to describe the radar echo [A7]. The

composite model has been assumed to hold for complex ocean waves as well, and is the basis of attempts to invert synthetic aperture radar (SAR) sea surface imagery to obtain directional wave spectral estimates. As pointed out by Wetzel [A8], however, it is not obvious that the more complicated small-scale structure developed in the open ocean can be described by Bragg scatter. Nonlinear features generated on the surface do not satisfy the mathematical constraints of the Rayleigh hypothesis, $ka < 1$, where k is the radar wave number and a is the sinusoidal component amplitude. Nonetheless, we invoke the Bragg-scatter composite model later for lack of another, to describe the scatter from the distributed roughness that lies along the greatest fractional area of the wave, away from the sharply defined wave crests. The crest scatter may be less important for moderate depression angles than for near grazing angles and probably contributes little from high-resolution radars because of the small surface area of such scatterers. For a high-resolution radar, however, breaking wave crests may cover a large fraction of a radar cell and contribute a significant percentage to the statistics of echo amplitudes. For example, σ^0 value of -30 dB in the 10° depression angle region of Fig. A1 results in a 0.1-m^2 cross section for a typical 100-m^2 scattering area for a marine radar. A single breaking crest can produce a 10-m^2 echo quite easily. Even for a much larger scattering patch, it is easy to see how crest features can contribute significantly to the total cross section.

The composite radar scatter model includes Bragg scatter as an element but allows this scatter from the small-scale structure to vary along the long-wave profile. This is caused by two mechanisms: geometric or tilt modulation, which simply describes the local small-scale structure being tilted by the long wave profile; and hydrodynamic modulation, which includes all fluid dynamic effects that cause the spectral density of the small-scale structure to vary along the long-wave profile. To this traditional composite scatter model, to accommodate our interests in low-grazing angle scatter, we add the broad range of effects that we label chaotic. These effects include wave breaking, which is particularly important near and just forward of the crests. This mechanism has not been treated by previous composite models but is necessary to describe the occurrence of sea spikes found in low grazing angle radar sea scatter.

Geometric or Tilt Modulation

Whereas the expression in Eq. (A1) holds for each wave component moving on a locally flat surface, the sea surface is composed of many wavelengths and heights. As a result, the local incidence angle at the surface is not the same as the depression angle at the radar but is modified by the local slope of the long wave at the point of radar illumination, as is seen in Fig. A3. Thus, the expression for the Bragg scatter amplitude given in Eq. (A1) requires this local incidence angle, which is the sum of the grazing angle and the slope angle of the long wave component, with slope measured positive as defined in Fig. A3.

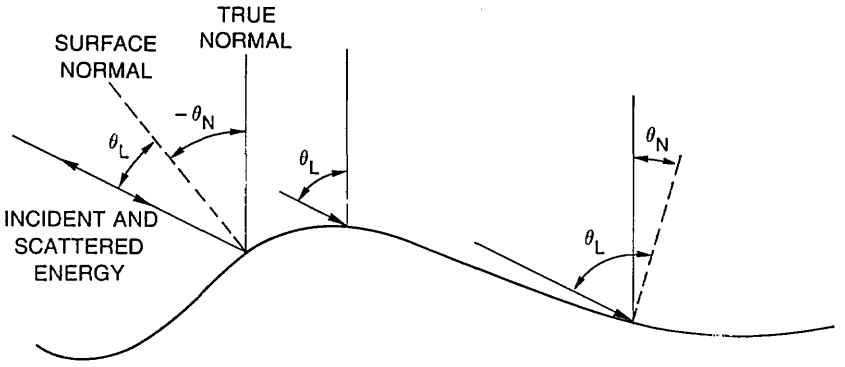

Fig. A3 — Local incidence angle of the radar signal is determined by the depression angle at the radar and the local slope of the long wave at the point of incidence and causes tilt modulation of the expression of Eq. (3)

For a collection of samples at a fixed delay and azimuth for a high spatial resolution radar, a large range of echo amplitudes results from tilt modulation. The NRCS samples forms a distribution of values given by Eq. (2) evaluated at angles between the sum of the depression angle at the radar plus and minus the maximum slope of the long wave illuminated. As an example, for a 7-s ocean wave of 75-m wavelength, the maximum long wave slope is arctan $[2\pi(h/2)/l] = 5°$, in effect the half-angle of the tilt modulation. Thus, for a grazing angle in the plateau region at 45°, local depression angles will vary between 40° and 50°. Using Fig. A3, the NRCS is modulated by this geometric effect between values of -18 and -15 dBm^2. For a grazing angle of 8°, the distribution of local grazing angles varies between 3° and 13°, resulting in a modulation of the NRCS of Fig. A1 of between -45 and -25 dBm^2, a significant increase in dynamic range. For very low grazing angles, the local incidence angle is varied from 0 (negative local incidence angles are cut off due to the onset of shadowing at 0°) to just above 5°. Because the NRCS plunges so strongly as 0° is approached, the receiver noise level is reached and limits the smallest NRCS observed. Nontheless, the variation in NRCS is largest at the lowest radar depression angles.

Since the variation of the local incidence angle along the long wavelength components of the ocean surface does not produce a severe variation in amplitude dynamic range for moderate incidence angles, a SAR image of the ocean surface can be recorded by using just a few bits of amplitude information. The marine radar, on the other hand, typically has ~60 dB of dynamic range to handle the wide range of echo power expected at low grazing angles.

Hydrodynamic Modulation

In addition to the geometric modulation, a hydrodynamic modulation also occurs. It is well known that the small-scale surface spectral density is modulated by the orbital wave motions of the long waves [A8]. Straining of small waves by long waves causes a shortening of the wavelength of the front face and a lengthening on the back face. A second type of modulation is that caused by sheltering of the wind by the wave profile, causing a variation in the local wind speed across the surface, with an expected smaller Bragg scatter density excited in the sheltered regions. The effect of each of these is to vary the amplitude of the Bragg scatterer spectral density of Eq. (A2) as a function of position on the long wave. These effects are typically dealt with empirically by definition of the modulation transfer function, introduced by Wright [A7]. The modulation transfer function is defined as

$$\sigma(x) = \sigma^0[1 + m(f)\,\eta(x)], \tag{A3}$$

where $\sigma(x)$ is the spatially varying NRCS of the sea-surface height, $\eta(x)$. It consists of a dc term, σ^0, and a spatially varying contribution that is proportional to the local sea-surface long-wave profile. This empirical expression assumes that the mapping from radar image to wave amplitude is linear for a given wave frequency, which has been shown to be true in wavetank experiments for moderate grazing angles. Such an empirical formalism does not hold for low grazing angles and open-ocean waves for reasons discussed in the text.

Chaotic Events, Including Wave Breaking

Recent results have shown that deterministic features on the surface may also contribute significantly to the NRCS of the sea surface for the higher grazing angles in which specular scatter may occur [A9], particularly for the very-high-resolution conditions encountered in wavetank studies in which a sharp surface crest feature can fill the illumination cell. For low grazing angles encountered by shipboard radars, scattering features are not expected to present specular scatter, but a type of double scatter can occur from plume-type breakers rolling down the front face of a propagating ocean

wave [A8]. The effect is not expected to be as dominant as in a wavetank, however, because the feature does not fill as large a fraction of the scattering cell in range or azimuth.

REFERENCES

A1. G.R. Valenzuela, "Theories for the Interaction fo Electromagnetic and Oceanic Waves—A Review," *Boundary-Layer Meteorology* **13**, 61-85 (1978).

A2. D.C. Crombie, "Doppler Spectrum of Sea Echo at 13.56 Mc/s," *Nature*, **175**, pp. 681-682 (1955).

A3. I.R. Young, W. Rosenthal, And F. Ziemer, "A 3-dimensional analysis of Marine Radar Images for the Determination of Ocean Wave Directionality and Surface Currents, *J. Geophys. Res.* **90** (C1), 1049-1059 (1985).

A4. J.P. Hansen and V.F. Cavaleri, "High Resolution Radar Sea Scatter, Experimental Observations and Discriminants," NRL Report 8557, Mar. 1982.

A5. I.D. Olin, "Amplitude and Temporal Statistics of Sea Spike Clutter," IEE Conf. Pub. 216, pp. 198-202, 1982.

A6. Lyzenga, D.R., A.L. Maffett, & R.A. Shuchman, "The Contribution of Wedge Scattering to the Radar Cross Section of the Ocean Surface," *IEEE Trans. Geosci. Remote Sens.*, **GE-21**, 502-505 (1983).

A7. J.W. Wright, "A New Model for Sea Clutter, *IEEE Trans. Ant. Prop.*, **AP-16**, 217-223, (1968).

A8. L.B. Wetzel, "A Model for Sea Backscatter Intermittency at Extreme Grazing Angles," *Radio Sci.*, **12**, 749-756, (1977).

A9. D.S.W. Kwoh and B.W. Lake, "A Deterministic, Coherent and Dual-Polarized Laboratory Study of Microwave Backscattering from Water Waves, Part 1: Short Gravity Waves without Wind," *IEEE J. Oceanic Eng.* **OE-9**, 291-308 (1984).

Appendix B

AIR-SEA INTERACTION PARAMETERIZATION

WIND STRESS — WIND SPEED — FRICTION VELOCITY RELATIONSHIPS

To interpret the apparent trends in the plots of radar parameters vs wind speed, it is useful to introduce the wind stress τ [B1]:

$$\tau = \rho \, <uw>, \tag{B1}$$

where ρ is the ratio of the air density to water density and $<uw>$ represents the correlation of the two horizontal components of the vector wind with the coordinate system taken as the x-axis along the wind direction. The wind friction velocity u_* is then defined by

$$u_*^2 = <uw> \tag{B2}$$

for purposes of bulk or large-area average parameterization of the air-sea interaction. The wind friction velocity is the large-area averaged value of the wind speed at the skin of the hypothetical average rough surface, defined so that the stress is uniformly distributed over that surface. The physical reality of such a quantity on a small scale is, of course, not meaningful in the case of a two-scale sea surface from which radar returns occur. Nevertheless, a formal definition can be made, considering the stress and friction velocity averaged over an area containing many large-scale wavelengths.

The friction velocity can be more effectively related to the normalized radar cross section (NRCS) cumulative distributions than to the wind speed for two reasons. First, the wind stress definition includes the effects of atmospheric stability or air-sea temperature differences. Second, the contributions to stress delivered from the wind to the surface can be broken up into several contributions, each of which may be able to be related to different contributions to the NRCS cumulative distributions. These wind stress contributions serve as some of the source and sink terms in the equation for wind wave generation and energy transfer between wave components of the wave spectrum [B2]. Intuitively, it would not be surprising for a relationship to exist between sea surface features/radar scattering mechanisms and individual surface stress contributions.

AIR-SEA TEMPERATURE DIFFERENCE EFFECTS

Air-sea temperature differences have been reported as an important parameter in the measure of mean NRCS for single wind speed [B3]. The effect of air-sea temperature difference in the wind stress definition can be taken into account by a drag coefficient C_D in a bulk parameterization of the wind friction velocity. The bulk method of measuring the wind stress assumes that the wind friction velocity defined at the surface can be related to the wind speed at an arbitrary height H through the drag coefficient

$$u_*^2 = C_D(H, T_a, T_s) \, U(H)^2 \tag{B3}$$

where $U(H)$ is the magnitude of the wind speed measured at an altitude H, and C_D is determined empirically. The drag coefficient is generally defined only for neutrally stable atmospheric conditions; for moderate winds it best fits an equation of the form

$$C_D = a + bU. \tag{B4}$$

Definition of the drag coefficient for unstable atmospheric conditions has only recently been done, and at least four different formulations are available for comparison [B3-B6]. If such a definition can be made successfully and if the spread in the radar parameters previously discussed is caused by the air-sea temperature difference dependence of the drag coefficient alone, the spread of the radar data is reduced significantly when plotted against wind friction velocity compared to the wind speed. The definition made by Keller et al. [B3] is not successful in reducing the spread of the mean RCS for X-band radar scatter at 45° incidence for measurements made in the Gulf of Mexico.

WIND STRESS AS THE SUM OF SEVERAL SEPARABLE CONTRIBUTIONS

Donelan [B7] has suggested that while the wind stress is a highly averaged quantity as formally defined, one can think of it as consisting of a sum of terms, each associated with different physical air-sea interaction processes. These are first broken into viscous drag τ_S and form drag contributions. The form drag is broken into terms related to production of surface currents τ_C and production of momentum in the form of surface waves. The momentum term further consists of a source term τ_M and a sink term τ_B relating to momentum lost through wave breaking. The final expression is simply the sum of

$$\tau_{Tot} = \tau_S + \tau_C + \tau_M + \tau_B. \tag{B5}$$

In particular, he has shown by simultaneous measurements of wave breaking and of the fluctuations of the water particle motions below the surface $< u'w' >$ that breaking waves deliver a significant fraction of momentum flux through the surface into the water, resulting in underwater turbulence. Phillips [B2] has further suggested that the contribution to the wind stress due to wave breaking can be a significant one under fully developed seas based upon theoretical considerations. We continue with this wavebreaking contribution to surface stress, following up on an observation by Jin Wu [B8].

Wu reanalyzed existing data in the literature on the wind speed dependence of percentage-area of whitecap coverage on the ocean surface and inferentially argued the reason for a dependence of the drag coefficient as wind speed to the one-half power to fit a 3.75 slope of log of whitecap coverage to wind speed. The argument was that the whitecap coverage should be proportional to the energy flux into the surface under equilibrium conditions. This energy flux is the product of the wind stress times the wind drift currents, the wind drift currents being also proportional to the wind friction velocity. Wu thus proposed the following dependence for the percentage area coverage by whitecaps W:

$$W \sim \tau u_* = \rho u_*^3 \sim (C_D U^2)^{3/2}. \tag{B6}$$

If one further assumes a wind speed dependence of the drag coefficient of U to the first power, as found by Large and Pond [B9], then one finds the energy flux and W proportional to $U^{4.5}$. To satisfy the observed whitecap coverage dependence of $U^{3.75}$, Wu had to postulate a wind friction velocity dependence on wind speed of $U^{0.5}$. Such a dependence agrees neither with the measurements of Large and Pond [B9] and others, nor with previously published work by Wu [B10].

REFERENCES

B1. H.U. Roll, *Physics of the Marine Atmosphere* (Academic Press, New York, 1965).

B2. O.M. Phillips, "Spectral and Statistical Properties of the Equilibrium Range in Wind-Generated Waves, I. Fluid Mech. **156**, 505-531 (1985).

B3. Keller, W.C., W.J. Plant, and D.E. Weissman, "The Dependence of X-band Microwave Sea Return on Atmospheric Stability and Sea State," *J. Geophys. Res.*, **90** 1019-1029 (1985).

B4. L.B. Wetzel, "On Microwave Scattering by Breaking Waves," in *Wave Dynamics and Radio Probing of the Ocean Surface,* O.M. Phillips and K. Hasselmann, ed. (Plenum Press, 1986 pp. 273-284.

B5. D.R. Lyzenga, A.L. Maffett, and R.A. Shuychman, "The Contribution of Wedge Scattering to the Radar Cross Section of the Ocean Surface, IEEE Trans. Geosci. Remote Sensing, **GE-21**, 502-505 (1983).

B6. Jin Wu, "Stability Parameters and Wind Stress Coefficients under Various Atmospheric Conditions," *J. Atmos. Oceanic Tech.*, (in press), 1986.

B7. M.A. Donlen, Whitecaps and Momentum Transfer, Turbulent Fluxes through the Sea Surface, Wave Dynamics, and Prediction, (Plenum Press, New York, 1978) pp. 273-287.

B8. Jin Wu, "Oceanic Whitecaps and Sea State, *J. Phys. Oceanog.*, **9**, pp. 1064-1068 (1979).

B9. W.G. Large and S. Pond, "Open Ocean Momentum Flux Measurements in Moderate to Strong Winds, *J. Phys. Oceanog.*, **11**, 324-336 (1981).

B10. Jin Wu, "Wind Stress Coefficients over Sea Surface Near Neutral Conditions—A Revisit, *J. Phys. Oceanog*, **10**, 727-740 (1980).